



# Visible light induced photocatalytic removal of Cr(VI) over TiO<sub>2</sub>-based nanosheets loaded with surface-enriched CoO<sub>x</sub> nanoparticles and its synergism with phenol oxidation

Dingze Lu<sup>a</sup>, Wuqiong Chai<sup>a</sup>, Minchen Yang<sup>a</sup>, Pengfei Fang<sup>a,\*</sup>, Wenhui Wu<sup>a</sup>, Bin Zhao<sup>a</sup>, Ruyue Xiong<sup>a</sup>, Hongmei Wang<sup>b</sup>

<sup>a</sup> Department of Physics and Key Laboratory of Artificial Micro- and Nano-Structures of Ministry of Education, Wuhan University, Wuhan 430072, PR China

<sup>b</sup> College of Biological, Chemical Sciences and Engineering, Jiaxing University, Jiaxing, Zhejiang 314001, PR China

## ARTICLE INFO

### Article history:

Received 10 January 2016

Received in revised form 29 February 2016

Accepted 2 March 2016

Available online 4 March 2016

### Keywords:

TiO<sub>2</sub>-based nanosheets

CoO<sub>x</sub> loading

Surface enrichment of CoO<sub>x</sub> nanoparticles

Cr(VI) removal

Simultaneous photodegradation with phenol

## ABSTRACT

Visible-light-driven (VLD) CoO<sub>x</sub> loaded TiO<sub>2</sub>-based nanosheets (Co-TNSs) with surface-enriched CoO<sub>x</sub> nanoparticles were successfully synthesized by using a facile one-pot hydrothermal method. The photocatalysts were characterized by SEM, AFM, HRTEM, XRD, Raman, XPS, FL and the surface photocurrent (SPC) technique, etc. The as-synthesized samples exhibit sheet-like structure with large specific surface area (260–350 cm<sup>2</sup>/g) and small thickness (3–4 nm). The CoO<sub>x</sub> nanoparticles (1–2 nm) are highly dispersed on the surface of TNSs. Loaded CoO<sub>x</sub> nanoparticles not only have influenced the crystal structure, crystallinity and surface area of the TNSs, but also resulted in considerable enhancement of visible-light (VL) absorption and a red-shift of the band gap of the TNSs. XPS results reveal that cobalt mainly exists in the form of Co<sup>2+</sup> and Co<sup>3+</sup>, and the binding energies of Ti–O bonds are changing with the loaded amount of CoO<sub>x</sub> nanoparticles. FL and SPC results indicate appropriate amount of CoO<sub>x</sub> (2.5 at.%) loading can effectively inhibit the recombination of photo-generated electron-hole pairs, thus improve the separation efficiency of charge carriers.

The photocatalytic activity of the samples was evaluated by the dichromate (Cr(VI)) solution under VL irradiation. It can be found that the Co-TNSs photocatalysts showed excellent VL photocatalytic activity for the removal of Cr(VI). Initially the photocatalytic activity increased with the content of CoO<sub>x</sub>, and then decreased after attaining a maximum value at an optimal content (2.5 at.%) for degradation of aqueous Cr(VI) solution. The addition of Ca<sup>2+</sup> promotes photocatalysis owing to its ionic bridging function in the form of =TiOH<sup>+</sup>–Cr(VI)–Ca<sup>2+</sup>–Cr(VI) linkages, while SO<sub>4</sub><sup>2–</sup> slightly inhibits the photo-reduction of Cr(VI), indicating good synergy of photocatalysis and adsorption even at higher ionic strength of electrolyte. The photocatalytic reduction of Cr(VI) is also significantly promoted by phenol and synergism between Cr(VI) reduction and degradation of phenol which is demonstrated by measuring the effect of multiple usage of Co-TNSs on its photocatalytic efficiency. Desorbed Co-TNSs (Co-TNSs-Des) are easily regenerated and reused for Cr(VI) removal with excellent performance. A possible alternate mechanism for the enhancement of photocatalytic activity under visible light irradiation is also proposed.

© 2016 Elsevier B.V. All rights reserved.

## 1. Introduction

The removal of toxic contaminants from water remains a huge challenge for industrial and municipal wastewaters as the deterioration of global environment is increasing. Wastewaters often

contain a lot of inorganic and organic pollutants. The major inorganic pollutants are heavy metals such as Cr, Pb, Hg and Cd ions, which have become a serious problem in the aquatic environment due to their toxicity, bioaccumulation and persistence [1–6]. And organic pollutants like phenol, polychlorinated biphenyls in water also have been causing serious environmental problems [7–9]. The co-existence of organic matter and metal ions in wastewater is a common phenomenon, such as leather tanning, film making, wood processing, automobile manufacturing, petroleum refining industry wastewater, etc. The simultaneous removal of organic

\* Corresponding author at: Department of Physics, Wuhan University, Wuhan 430072, Hubei, PR China.

E-mail addresses: [fangpf@whu.edu.cn](mailto:fangpf@whu.edu.cn), [fpf.whu@163.com](mailto:fpf.whu@163.com) (P. Fang).

matter and metal ions from wastewater has particular significance to pollution control and remediation. Among various treatments of removing the pollutants from wastewaters, photocatalytic technology is known as a promising one due to its ability to mineralize most of the organic pollutants by using only luminous energy.  $\text{TiO}_2$  has been proved to be the most representative and extensively used photocatalyst, owing to its high photo-activity, low cost, non-toxicity, high oxidation ability and relatively high chemical stability [10,11]. However, its relatively wide band gap ( $\sim 3.2$  eV) and the high recombination rate of the photo-generated electron-hole pairs hinder its large-scale applications [12,13]. Therefore, considerable efforts have been made to narrow the band gap to shift the absorption edge of  $\text{TiO}_2$ -based materials, deeper into the visible-light (VL) region of the electromagnetic spectrum, where the Sun's total irradiance lies nearly 42%.

To reach this goal, one of the challenges is to develop highly effective photocatalysts to accelerate the reactions. Recently, the manipulation of morphology of  $\text{TiO}_2$ -based photocatalysts has attracted attention of many researchers. As a result,  $\text{TiO}_2$  has been reported in different morphologies in recent years, e.g., nanofibers, nanotubes, nanorods, nanosheets, and nanoflowers owing to their large specific surface area and small dimension effect [14–19]. Larger specific surface area allows photocatalysts to expose for the light effectively and lead better contact with more molecules of pollution thus efficient photocatalytic reaction. Smaller thickness of photo catalyst may be beneficial to improve the separation rate of photo-generated electron-hole pairs. Inspired by the natural photochemical process by leaves of plants with their two-dimensional (2D) structure that can efficiently convert sunlight to chemical energy through photosynthesis, developing and improving 2D  $\text{TiO}_2$ -based nanomaterial have attracted increasing attentions [20,21]. Comparing with other morphologies of  $\text{TiO}_2$ -based photocatalysts, 2D-nanosheets possess higher specific surface area and smaller thickness. These advantages make nanosheets be expected to exhibit excellent photocatalytic activity. Various methods have been attempted for the preparation of nanosheets so far, such as hydrothermal method, sol-gel method, chemical vapor decomposition (CVD) methods, etc. [22–26]. Hydrothermal method is one of the most popular methods due to its advantages of simpleness and convenience.  $\text{TiO}_2$  nanoparticles (3D) take the form of nanosheets (2D) and finally nanotubes (1D) under hydrothermal conditions. Controlling the environment of the reaction, results in the synthesis of different nanostructures of  $\text{TiO}_2$ -based nanomaterial [27]. Our previous work shows that,  $\text{TiO}_2$ -based nanosheets (TNSs) with high specific surface area ( $339 \text{ m}^2/\text{g}$ ) can be synthesized and the thickness of single nanosheet has reached to 4–5 nm. Moreover, UV–vis photocatalytic efficiency of TNSs is better than Degussa P25 during the degradation of Rhodamine B (RhB), methylene blue (MB), crystal violet (CV), etc. [27,28].

However, the photocatalytic efficiency of pure  $\text{TiO}_2$ -based nanosheets was relatively low, particularly under VL irradiation, due to the fast recombination rate of electron-hole pairs. In order to enhance the interfacial charge-transfer efficiency and utilize wider spectral range of solar energy, the  $\text{TiO}_2$ -based nanosheets catalyst has been modified by doping and manipulating nanomaterial composition [29,30]. Till date numerous efforts have been devoted to increase the separation efficiency of photo-generated charges and expand spectral response into VL region. Majority of the studies are focused on the modification of photocatalysts with metal and nonmetal additives as well as organic photo sensitizers [31–33]. Loading  $\text{TiO}_2$ -based nanosheets with  $\text{CoO}_x$  nanoparticles may be an efficient method to obtain high photocatalytic activity under VL irradiation owing to the photosensitizing effect of the  $\text{CoO}_x$  nanoparticles with narrow energy gap. The  $\text{CoO}_x$  nanoparticles promote photosensitization, leading to the enhanced activity. However, these tiny  $\text{CoO}_x$  nanoparticles may easily

suffer from leaching and runoff, leading to the poor durability. The structure and morphology of photocatalyst have received increasing attention owing to their remarkable influence on both the reactant adsorption and light absorbance. Meanwhile, the unique structure and morphology might also play key roles in determining the dispersion and the stability of loading against leaching during photocatalytic reactions.

In the present work, a novel visible-light-driven (VLD)  $\text{CoO}_x$  loaded TNSs with surface-enrich  $\text{CoO}_x$  nanoparticles with high photocatalytic activity were successfully synthesized by a facile one-pot hydrothermal approach. The  $\text{CoO}_x$  nanoparticles are highly dispersed on the surface of  $\text{TiO}_2$ -based nanosheets. The photocatalytic activities of the resultant Co-TNSs were evaluated by simultaneous photocatalytic detoxification of Cr(VI) and degradation of phenol. The Cr(VI) was selected as a reference metal ion since it is one of the most toxic ions present in the environment, posing toxicity to most organisms at the concentrations of higher than 0.05 ppm. Wastewaters generated from various industries contain aromatic compounds (e.g., Phenol, etc.) and their derivatives are toxic and thus have adverse effects on health and environment. Moreover, phenol has been known as an electron donor in the photocatalytic system; hence, phenol was selected as the oxidizable organic compound in a simultaneous photocatalytic oxidation-reduction reaction. The strong synergistic effect was demonstrated by simultaneous decontamination of Cr(VI) and phenol.

## 2. Materials and methods

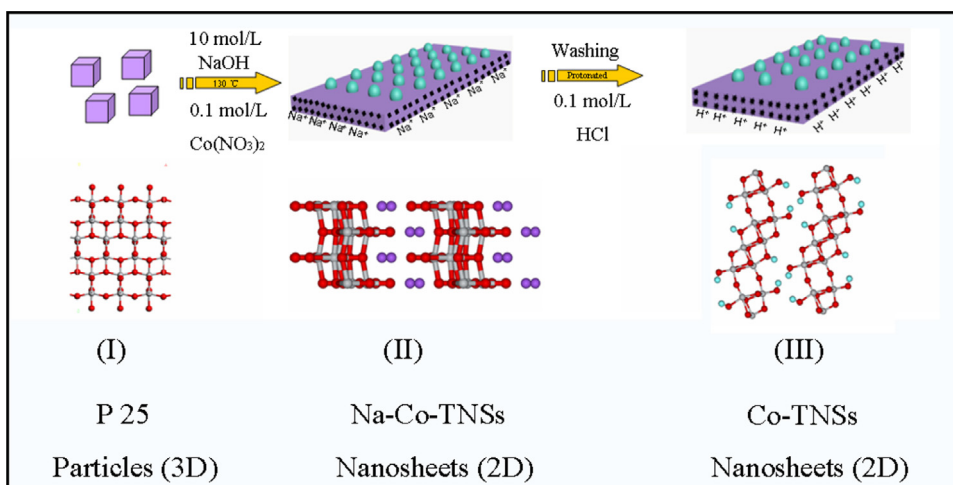
### 2.1. Preparation of photocatalysts

Degussa P25 ( $\text{TiO}_2$ , 80% anatase, 20% rutile) is the product of Degussa Co., Ltd. The NaOH, cobalt nitrate ( $\text{Co}(\text{NO}_3)_2$ ),  $\text{HNO}_3$ , acetone ( $\text{C}_3\text{H}_6\text{O}$ ), phosphoric acid ( $\text{H}_3\text{PO}_4$ ), 1, 5-diphenylcarbohydrazide ( $\text{C}_{13}\text{H}_{14}\text{N}_4\text{O}$ ), ethyl alcohol ( $\text{C}_2\text{H}_5\text{OH}$ ),  $\text{H}_2\text{O}_2$ , phenol, potassium dichromate ( $\text{K}_2\text{Cr}_2\text{O}_7$ ), ammonium chloride ( $\text{NH}_4\text{Cl}$ ), 4-amino-antipyrine ( $\text{C}_{11}\text{H}_{13}\text{N}_3\text{O}$ ),  $\text{K}_3[\text{Fe}(\text{CN})_6]$  solution were provided by Sinopharm Chemical Reagent Co., Ltd, and coumarin was obtained from Alfa Aesar. All of the reagents were at analytically pure level and used without any further purification. Deionized (DI) water with a resistance of  $4.25 \text{ M}\Omega \text{ cm}$  was used in all experiments.

In a typical preparation procedure as shown in Scheme 1, 0.8 g P25 was dispersed in 50 mL of 10 mol/L NaOH solution under intense stirring. A certain amount of cobalt nitrate solution was dropped slowly into the suspension. After magnetically stirred for 1 h, the mixture was treated at  $130^\circ\text{C}$  for 3 h in a 100 mL Teflon-lined autoclave. After the reaction, the autoclave was cooled down to the room temperature by water-cooling. The resultant white powders were washed with DI water until their pH reached 7, and followed by the proton exchange in 200 mL of diluted HCl solution. Finally, the powders were treated with DI water for several times and then dried at  $70^\circ\text{C}$  for 12 h. The obtained samples were denoted by x-Co-TNSs, where x ( $x = 0.5\%$ ,  $1.0\%$ ,  $1.5\%$ ,  $2.0\%$ ,  $2.5\%$ ,  $3.0\%$ ,  $3.5\%$ ,  $4.0\%$ , and  $5.0\%$ ) representing the concentration of cobalt nitrate in the precursor solution. For comparison, unloaded  $\text{TiO}_2$ -based nanosheets (TNSs) were also prepared using the same process without adding any cobalt source.

### 2.2. Characterization of photocatalysts

The morphological features of the specimens were characterized by scanning electron microscopy (SEM) (SIRION, FEI, Netherlands), transmission electron microscopy (TEM) on JEOL TEM-2010 (HT) instrument, and high-resolution transmission electron microscopy (HRTEM) on JEM-2010 FEM. An atomic force



**Scheme 1.** Schematic illustration of surface-enriched  $\text{CoO}_x$  nanoparticles loaded  $\text{TiO}_2$ -based nanosheets synthesized by a facile one-pot hydrothermal.

microscopy (AFM) was used to examine the surface morphology and thickness of samples. The measurement was carried out in a tapping model, with a driving frequency of 130 kHz at a scan speed of 0.4 Hz using a silicon cantilever with a normal spring constant of  $16 \text{ N m}^{-1}$ . The specific surface areas ( $S_{\text{BET}}$ ) were measured by obtaining nitrogen adsorption-desorption isotherm at 77 K using the instrument (JW-BK122W, China). The results of X-ray diffraction (XRD) were collected on Bruker D8 advance X-ray diffractometer by  $\text{Cu K}\alpha$  radiation and the accelerating voltage and current were 40 kV and 40 mA, respectively. The results were obtained with a step of  $0.02^\circ$  in the range ( $2\theta$ ) from  $20^\circ$  to  $80^\circ$ . Raman spectra were obtained by Horiba Lab RAM HR Raman spectrometer with an excitation wavelength of 448 nm. UV-vis diffuse reflectance spectra (DRS) of the samples were measured using Shimadzu UV-2550 spectrometer equipped with a diffuse reflectance attachment with a  $\text{BaSO}_4$ -coated integrating sphere against a  $\text{BaSO}_4$  reference. X-ray photoelectron spectroscopy (XPS, Thermo Fisher ESCALAB 250Xi) was utilized to analyze the chemical composition of samples and the valence states of various elements. The binding energies were referenced to the C 1s at 284.6 eV. Acq method was applied by the software of XPS Peak 4.1 and the spectra were analyzed by carrying out a Shirley background subtraction. The actual chemical compositions were measured by inductively coupled plasma atomic emission spectrometry (ICP-AES; Optima 4300 DV, USA). The fluorescence (FL) spectra were surveyed by a Hitachi FL 4600 using the PMT voltage of 700 V to study the recombination efficiency of photo-generated electrons and holes.

### 2.3. Measurements of photocatalytic performance

#### 2.3.1. Evaluation of dichromate ( $\text{K}_2\text{Cr}_2\text{O}_7$ ) solution

The photocatalytic reduction of aqueous Cr(VI) to Cr(III) was performed at  $25^\circ\text{C} \pm 2^\circ\text{C}$  by a 200 mL quartz reactor containing 100 mg photocatalyst and 100 mL of Cr(VI) aqueous solution at a concentration of 50 ppm. The pH values of reacting solutions were adjusted with HCl or NaOH solution. Without any additives, the pH value of the suspension was found to be at around 6.8. Adsorption was monitored in the darkness while periodically withdrawing a small amount of solution (0.2 mL) provided a continuous dilution, complexing, and measurement. Once reaching the adsorption-desorption equilibrium, the reactor was exposed to a 300 W Xe lamp ( $172 \text{ mW/cm}^2$ , 15 cm away from the photocatalytic reactor). The total duration of the reaction process was 140 min. For every 20 min, 0.8 mL of solution was collected and centrifuged for 2 min to separate the photocatalyst at a speed of 1200 r/min. The

final samples were obtained by 0.4 mL of supernatant liquor mixed with 2.8 mL of deionized water. The Cr(VI) content in the supernatant solution was analyzed colorimetrically at 540 nm using the diphenylcarbazide method (DPC) by UV-vis spectrometer. When the photocatalytic activity was evaluated under VL irradiation, a cut-off filter ( $\lambda \geq 420 \text{ nm}$ ) was kept on the top of the apparatus.

#### 2.3.2. Evaluation of simultaneous photocatalytic decontamination of Cr(VI) and phenol

Simultaneous photocatalytic reaction was carried out at  $25^\circ\text{C} \pm 2^\circ\text{C}$  in a 200 mL quartz reactor containing 100 mg photocatalyst and 100 mL aqueous solution of phenol suspension and Cr(VI) ion at 20 ppm and 50 ppm, respectively. The pH value of the solution was controlled at 3.0 by the addition of HCl solution. The reacting suspensions were stirred in darkness for 1 h to make sure that the adsorption-desorption equilibrium has been established before the photocatalytic reaction. The Xe lamp was turned on subsequently. The whole reaction process lasted 140 min. The Cr(VI) content in the supernatant solution was measured colorimetrically at 540 nm using the DPC method by UV-vis spectrometer. The phenol content in the supernatant solution was analyzed colorimetrically at 510 nm by UV-vis spectrometer. A calibration based on Beer-Lambert law was used to quantify the concentration. Besides, Cr(VI) content, Cr(III) content, and total Cr content were also analyzed by ICP-AES (Optima 4300 DV, USA).

### 2.4. Surface photocurrent (SPC) and electrochemical impedance spectra (EIS) experiments

Initially, 5 mg of TNSs or  $\text{CoO}_x$ -loaded TNSs were dispersed in 5 mL ethanol, respectively. Through sonication for about 90 min, the slurries were dip-coated onto an indium-tin oxide (ITO) glass electrode ( $1 \times 2 \text{ cm}$ ) and then dried at  $50^\circ\text{C}$  for 5 h. During the investigations, the as-prepared photocatalyst/ITO electrodes, the saturation calomel electrode and platinum electrode were employed as the working electrode, reference electrode and counter electrode, respectively.  $\text{Na}_2\text{SO}_4$  aqueous solution with the concentration at 1 M was chosen as electrolyte. The working electrode (the prepared photocatalyst/ITO electrodes) was irradiated horizontally by a high pressure Xe lamp (300 W) equipped with a cutoff filter ( $\lambda \geq 420 \text{ nm}$ ). The distance between working electrode and Xe lamp was kept at 15 cm. The surface photocurrent (SPC) tests in the experiments were performed by the electrochemical workstation (CHI-660C, Chenhua, China). Similarly, the electrochemical impedance spectra (EIS) were also measured by the same

electrochemical system (CHI-660C, Chenhua, China). Na<sub>2</sub>S solution (0.1 M) was used as the electrolyte solution. The VL irradiation was obtained from a 300 W Xe lamp with a 420 nm cut off filter.

### 2.5. Analysis of photo-generated hydroxyl radicals ( $\bullet$ OH)

The formation of  $\bullet$ OH radicals on the illuminated photocatalysts was analyzed by the photoluminescence (PL) technique using coumarin (COU) as a probe molecule. COU can readily react with  $\bullet$ OH to form highly fluorescent COU-OH adducts (7-hydroxycoumarin). The PL intensity of 7-hydroxycoumarin (7-HC) was proportional for the amount of  $\bullet$ OH radicals formed on the surface of the photocatalysts [27,29]. The cut-off filters ( $\lambda \geq 420$  nm) were used to obtain VL. The reaction suspensions were carried out by adding photocatalyst (0.2 g) into aqueous COU solution (1 mM, 100 mL). The suspensions containing COU as well as photocatalyst powder are magnetically stirred in dark for an hour to establish an adsorption-desorption equilibrium and then were irradiated by 300 W Xe lamp under constant air-equilibrated conditions. At the given time intervals of 5 min, PL spectra of 7-HC product were detected on a fluorescence spectrophotometer (Hitachi F-4600). The increase in the PL intensity at 450 nm of 7-HC by excitation with a wavelength of 342 nm was measured.

### 2.6. Materials reuse

After the adsorption-photocatalysis process, the nano materials were separated by vacuum filtration using a 0.22 mm membrane from Cr(VI)-phenol coexisted systems of pH = 3. After dried in air, the separated materials of 0.2 g L<sup>-1</sup> were soaked in HNO<sub>3</sub> solutions (0.5 M) for 8 h to desorb Cr(III), and then the desorbed materials were separated and washed with DI water until the leachate to neutral. Finally, the desorbed materials were carried out by photocatalytic degradation to regenerate as follows. About 0.1 g Cr-desorbed 2.5%-Co-TNSs (collected after the desorption experiments) was added into 50 mL of DI water under intense stirring, and then 2 mL of 30% H<sub>2</sub>O<sub>2</sub> solution was dropped into the suspension to accelerate the degradation of phenol. After irradiated with a 300 W high-pressure Xe lamp for 6 h, the photocatalyst was separated by centrifugation and used for the next photocatalytic cycle test. The whole process of photocatalysis adsorption, desorption, and regeneration was continuously run for 7 cycles, and conducted in triplicate. To investigate the reusability efficiency of the nano-material, 0.1 g L<sup>-1</sup> desorbed and regenerated materials were reused in the Cr(VI)-phenol coexisted experiments with an initial phenol concentration of 20 ppm and Cr(VI) concentration of 50 ppm at pH = 3. In addition, the 2.5%-Co-TNSs sample was characterized by transmission electron microscopy (TEM) and high-resolution transmission electron microscopy (HRTEM) for morphology, X-ray diffraction (XRD) for crystal structure, X-ray photoelectron spectroscopy (XPS) and Raman spectra, after photocatalysis-adsorption followed by desorption and regeneration.

## 3. Results and discussion

### 3.1. Morphology, microstructure and chemical state of the CoO<sub>x</sub>/TNSs photocatalysts

Fig. 1a, c, e and g depicts the TEM images of P25, TNSs, 2.5%-Co-TNSs, and 5.0%-Co-TNSs samples. As shown in Fig. 1a, the pristine TiO<sub>2</sub> products have a granular morphology and the granules are nearly mono dispersed in size of dozens of nanometers. Uniform clusters of nanosheets were formed after hydrothermal treatment at 130 °C for 3 h (Fig. 1b), which is consistent with the previous reports [28,34]. The samples mainly possess nanosheets of length greater than one hundred nanometers and the width

of several tens of nanometers. The increasing the dimensions of nanosheets implies that the small nanosheets stripped off from the granular crystals, due to the oxolation of the OH species at the edge of raw nanosheets [35,36]. The formation of TNSs can be ascribed to the exfoliation of granular TiO<sub>2</sub> into sheet-like structure under alkaline hydrothermal conditions. During the reaction, plenty of Ti–O bonds of P25 are broken, causing the split of TiO<sub>2</sub> nanoparticles. As a consequence, the TiO<sub>2</sub> nanoparticles are stripped into smaller planar nanosheets. Finally, these smaller planar nanosheets join together to form larger planar nanosheets. Fig. 1e and g shows the TEM image of 2.5%-Co-TNSs and 5.0%-Co-TNSs, respectively. It can be seen that 2.5%-Co-TNSs and 5.0%-Co-TNSs have showed sheet-like structure. In other words, the nanosheet structure was not destroyed even after introducing cobalt source in the hydrothermal reaction. In addition, TiO<sub>2</sub>-based nanosheets possess low thickness (ca. 3.6 nm) which is much lower than that of the raw TiO<sub>2</sub> nanoparticles as shown in Fig. S1. The thinness of nanosheets leads to a decrease in the diffusion path of photo-generated carriers, reaching to the surface of nanosheets, which may be beneficial to the enhancement of separation rate of photo-generated electron-hole pairs.

In order to further study the morphological features of the specimens, SAED pattern, high-resolution TEM images and EDS of as-prepared specimens are monitored. The SAED pattern possesses diffraction lines which indicate the polycrystalline phases, namely, (1 0 1), (0 0 4), (2 0 0), (2 0 4), (2 1 5) diffractions of anatase phase and (2 1 1), (1 1 2) diffractions of rutile phase. When compared the SAED pattern of TNSs with that of P25, the initial diffraction rings all disappeared and some new diffraction rings with less distinct were observed, indicating the change of crystal structure and a poor crystallinity. Alvarez-Ramirez et al. suggest that P25 TiO<sub>2</sub> powders react with NaOH solution to form highly disordered TiO<sub>2</sub>-based nanosheets under the hydrothermal conditions (130 °C, 3 h), TiO<sub>2</sub> nanoparticles are stripped into thin lamellar fragments [37]. After the process of stripping to a certain extent, large amounts of Ti–O bonds are broken to form TiO<sub>2</sub>-based nanosheets. The transformation from TiO<sub>2</sub> nanoparticles (3D) to TiO<sub>2</sub>-based nanosheets (2D) is gradual; it proceeds from surface region and then extends to bulk. Initially the Ti–O bonds on the surface are broken. During the breaking process of Ti–O bonds, the O atoms are twisted or rotated, creating an angle between Ti and O atoms. It can lead to the formation of the lepidocrocite-type layers, which are suggested to be the construction units in any layered titanate. Then, the thin lamellar fragments link with each other to form larger planar nanosheets. In addition, the HRTEM images of P25, TNSs, 2.5%-Co-TNSs, and 5.0%-Co-TNSs are presented in Fig. 1b, d, f and h). Comparing with P25, as-synthesized TNSs, 2.5%-Co-TNSs, and 5.0%-Co-TNSs do not have well-developed lattice fringes or other typical crystal characteristics, showing relatively low crystallinity. From Fig. 1d, f and h, it can be seen that Co-TNSs have the similar sheet-like structure with the bare TNSs. In addition, it can be found that the surface of 2.5%-Co-TNSs (Fig. 1f) is much rougher than that of bare TNSs. When the loaded ratio of Co/Ti is at 5.0 at.%, small particles (about 1–2 nm) appeared on the surface of TNSs, which is the direct evidence for the loaded cobalt oxides (CoO<sub>x</sub>). The EDS (the insets) in Fig. 1f and h exactly support the point, and the distinct peaks ascribes to Ti, O, and Co, confirming the corresponding elements in the composites.

N<sub>2</sub> adsorption-desorption isotherms and pore size distribution of P25, TNSs, 2.5%-Co-TNSs and 5.0%-Co-TNSs are measured to analyze their porous properties. As shown in Fig. S2a, the N<sub>2</sub> adsorption-desorption isotherms of TNSs belong to a typical Type IV sorption behavior with a large Type H3 hysteresis loop, which represents the mesoporous structure according to the classification of IUPAC and the mesopores mainly origin from the interspaces of the aggregated nanosheets [38]. The hysteresis loops are also observed in x-Co-TNSs (x = 1.0%, 2.0%, 3.0%, and 4.0%), and the



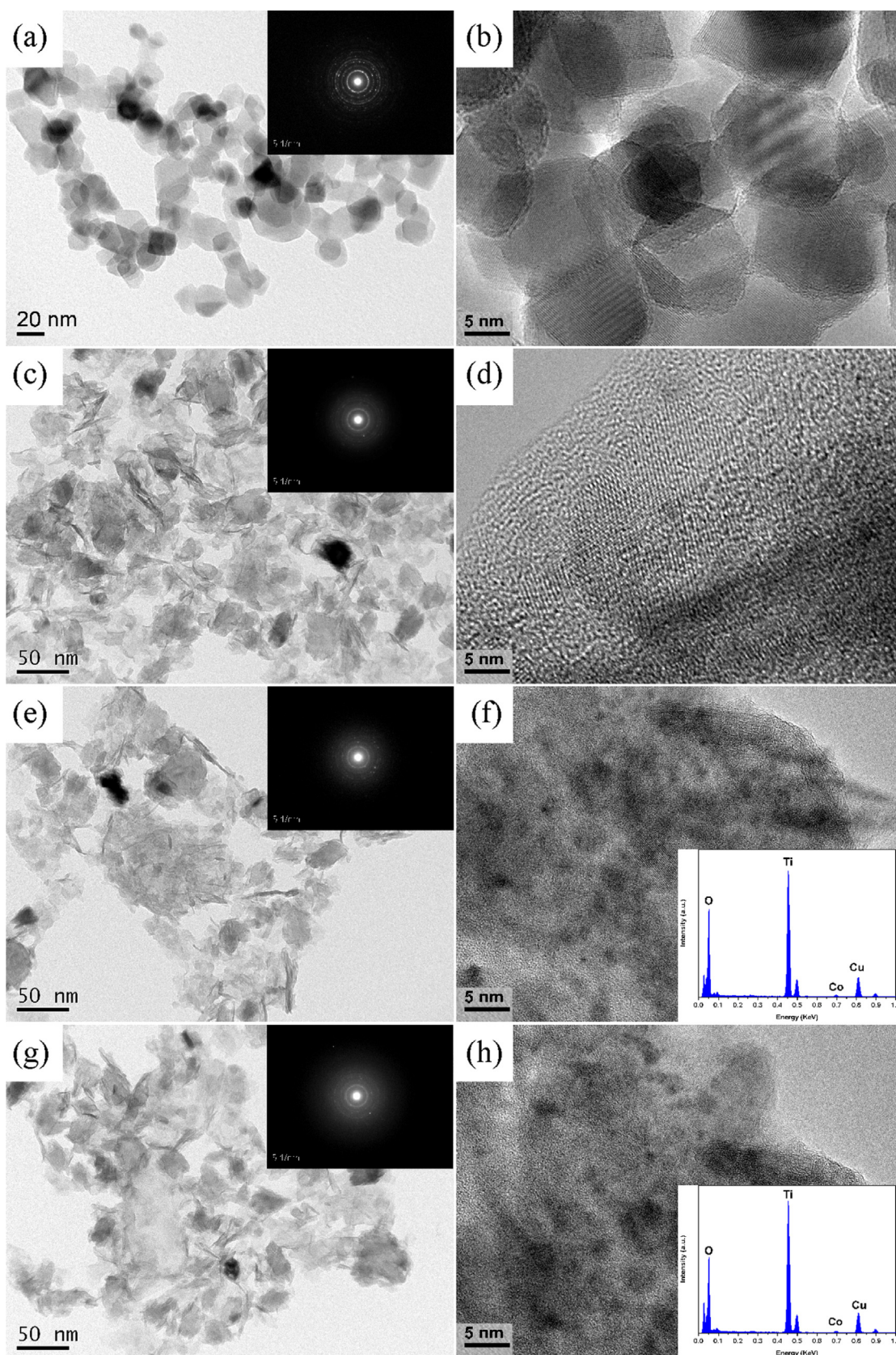


**Fig. 1.** TEM images, partial SAED patterns, HRTEM images, and EDS spectra of the P25, TNSs and CoO<sub>x</sub> loaded TNSs for (a–b) P25, (c–d) TNSs, (e–f) 2.5%-Co-TNSs, and (g–h) 5.0%-Co-TNSs.

**Table 1**

Structure parameter of P25, undoped TNSs and Co-TNSs composites.

Samples notation	Co/Ti molar ratio	$S_{\text{BET}}$ ( $\text{m}^2/\text{g}$ )	APS <sup>a</sup> (nm)	PV <sup>b</sup> ( $\text{cm}^3/\text{g}$ )	BE <sup>c</sup> (eV)	FWHM <sup>d</sup> ( $\text{cm}^{-1}$ )
P25	0.0%	52.41	7.31	0.151	3.22	8.21
TNSs	0.0%	349.25	10.08	0.891	3.21	13.21
0.5%-Co-TNSs	0.5%	338.16	9.93	0.887	3.19	13.15
1.0%-Co-TNSs	1.0%	329.38	10.05	0.881	3.13	13.11
1.5%-Co-TNSs	1.5%	317.79	10.54	0.873	3.08	13.04
2.0%-Co-TNSs	2.0%	299.46	9.97	0.861	3.07	12.94
2.5%-Co-TNSs	2.5%	287.85	9.89	0.847	3.03	12.86
3.0%-Co-TNSs	3.0%	278.23	12.19	0.828	2.98	12.79
3.5%-Co-TNSs	3.5%	268.52	13.29	0.816	2.96	12.75
4.0%-Co-TNSs	4.0%	259.46	13.68	0.809	2.95	12.71
5.0%-Co-TNSs	5.0%	254.63	15.81	0.805	2.90	12.69

<sup>a</sup> The average pore size.<sup>b</sup> The BJH total pore volume.<sup>c</sup> The band-gap energy.<sup>d</sup> The FWHM of Raman peak.

Co-TNSs samples show a lower absorption than bare TNSs at high relative pressure range ( $0.60 < P/P_0 < 0.99$ ), indicating a decrease in the mesopores (Fig. S2b). Co-TNSs exhibit an average pore size with a narrow distribution, which is a slightly lower than that of TNSs. That can be attributed that the small  $\text{CoO}_x$  nanoparticles dispersed into the pores of TNSs. The results were also confirmed by the decreasing tendency of  $S_{\text{BET}}$  from  $349.25 \text{ m}^2/\text{g}$  of TNSs to  $254.63 \text{ m}^2/\text{g}$  of 5.0%-Co-TNSs (Table 1). These results suggest that the  $\text{CoO}_x$  nanoparticles enter into the interspaces of the aggregated nanosheets due to ion-exchange that took place during hydrothermal process and block the mesopores among them and thus decrease  $S_{\text{BET}}$  as well as pore volume of TNSs.

The crystallization of P25, TNSs and x-Co-TNSs ( $x = 0.5\%$ ,  $1.0\%$ ,  $1.5\%$ ,  $2.0\%$ ,  $2.5\%$ ,  $3.0\%$ ,  $3.5\%$ ,  $4.0\%$ , and  $5.0\%$ ) were further identified by wide angle X-ray diffraction patterns. As shown in Fig. 2a, P25 exhibits a mischcrystal of anatase (JCPDS No. 89-4921) and rutile (JCPDS No. 89-0552) phase. Comparing with the spectra P25 and TNSs, it can be found that original peaks were weakened markedly, indicating that as-synthesized TNSs after alkaline hydrothermal treatment are not well crystallized. It is well known that the sodium titanates are first formed from high-crystalline titania powder through hydrothermal treatment, and then the sodium titanate products transform to hydrogen titanate with poor crystalline characteristics after washing with HCl solution [39,40]. Some characteristic peaks disappear, suggesting that there occurs a transformation from 3D crystal structure of  $\text{TiO}_2$  to 2D  $\text{TiO}_2$ -based nanosheets during the hydrothermal reaction. Moreover, XRD patterns of Co-TNSs with different ratio of Co/Ti are substantially similar. However, the intensities of  $A(101)$ ,  $R(110)$ ,  $A(200)$ , and  $A(105)$  patterns increased slightly and the corresponding full widths at half maximum (FWHM) values become narrower as the loaded amount of  $\text{CoO}_x$  nanoparticles increasing, suggesting that the loaded  $\text{CoO}_x$  nanoparticles may somewhat affect the transformation from P25 (3D) to  $\text{TiO}_2$ -based nanosheets (2D). However, the XRD spectra do not show the characteristic peaks of  $\text{CoO}_x$ . Actually, for  $\text{CoO}_x$  being not observed, there are two cases: one is that  $\text{CoO}_x$  does not exist in the product; the second is that amorphous  $\text{CoO}_x$  has been formed. To this end, we have made further investigations which are given in supplementary information and the results are shown in Fig. S3. From the analysis results, it can be concluded that introduced cobalt mainly confined to the surface of TNSs in the form of amorphous oxides ( $\text{CoO}_x$ ).

To further study the transformation of the structure, the Raman spectra of the samples are verified. Fig. 2b presents Raman spectra of P25 and bare TNSs. The patterns clearly display Raman peaks in the range of  $100\text{--}800 \text{ cm}^{-1}$ . The peaks at around  $147 \text{ cm}^{-1}$  ( $E_g$ ),  $197 \text{ cm}^{-1}$  ( $E_g$ ),  $399 \text{ cm}^{-1}$  ( $E_g$ ) and  $643 \text{ cm}^{-1}$  ( $E_g$ ) are the characteristics of anatase phase [41,42]. Comparing with spectra of

P25 and bare TNSs, it can be found that hydrothermal treatment ( $10 \text{ M}$ ,  $130^\circ\text{C}$ ) made all original peaks significantly weaken (in the spectrum of TNSs). Two new peaks at around  $279 \text{ cm}^{-1}$  ( $B_{1g}$ ) and  $456 \text{ cm}^{-1}$  ( $E_g$ ) appeared, which were ascribed to titanate [43]. As is well known that the sodium titanates may firstly be formed from raw titania powder through hydrothermal treatment; the formed sodium titanate products were convert to titanate subsequently through washing with  $0.1 \text{ M}$  of HCl solution for  $3 \text{ h}$  [28,39]. Meanwhile, a large number of hydroxyls groups may generate on the surface of TNSs through an ion exchange process. The formed OH groups can effectively enhance the adsorption of pollutants onto adsorbents. The insert of Fig. 2b shows Raman spectra of  $\text{CoO}_x$  loaded TNSs with various Co/Ti ratios. From the spectra of Co-TNSs with different Co/Ti ratio, it can be found that the relative intensity of the main  $E_g$  mode ( $141 \text{ cm}^{-1}$ ) increases gradually with the loaded amount of  $\text{CoO}_x$  nanoparticles increasing from  $0.0 \text{ at.}\%$  to  $5.0 \text{ at.}\%$ . The intensity of  $E_g$  mode ( $141 \text{ cm}^{-1}$ ) of the 5.0%-Co-TNSs is 3.45-fold to that of bare TNSs, indicating that loaded  $\text{CoO}_x$  nanoparticles could affect the transformation from P25 (3D) to  $\text{TiO}_2$ -based nanosheets (2D) which is in agreement with the XRD results. The Raman spectra were also analyzed by Lorentzian and Gaussian multi peak fitting. With the loaded amount of  $\text{CoO}_x$  nanoparticles increasing, the general trend in the value of FWHM of the main  $E_g$  mode ( $\sim 141 \text{ cm}^{-1}$ ), a decrease from  $15.98$  to  $14.32 \text{ cm}^{-1}$  can be observed. In addition, main  $E_g$  mode ( $\sim 141 \text{ cm}^{-1}$ ) also shows the weak frequency shift (the insert of Fig. 2b). The decrease of FWHM and the weak frequency shift of the main  $E_g$  mode suggested that the  $\text{CoO}_x$  loading may influence Ti–O lattice vibration.

The surface composites and chemical states of the samples were then studied by XPS. As shown in Fig. 3a, the XPS survey spectra exhibit the characteristic peaks of Ti, O, Co and C elements. The spectrum is calibrated with respect to the peak of C element. In Fig. 3b, the broad and asymmetric O 1s core level spectra of TNSs was fitted by two Gaussian peaks at around  $530.02 \text{ eV}$  and  $531.58 \text{ eV}$  which can be attributed to Ti–O and hydroxyl oxygen, respectively [44,45]. After loading  $\text{CoO}_x$  nanoparticles, O 1s core level spectra of 2.5%-Co-TNSs and 5.0%-Co-TNSs shifted towards higher binding energies by  $0.1 \text{ eV}$  and  $0.15 \text{ eV}$ , respectively, suggesting the form of Ti–O–Co bonds [46,47]. It can be inferred that the loaded  $\text{CoO}_x$  could exist on the surface of TNSs via Ti–O–Co bonds at the interface. Fig. 3c shows the XPS spectra of the Ti 2p region. The Ti  $2p_{3/2}$  and Ti  $2p_{1/2}$  peaks are located at  $\sim 464$  and  $\sim 458 \text{ eV}$ , respectively. The Ti 2p peak of 2.5%-Co-TNSs and 5.0%-Co-TNSs were shifted towards higher BE by  $0.3 \text{ eV}$  and  $0.7 \text{ eV}$  respectively with the loaded amount of  $\text{CoO}_x$  nanoparticles, which can be ascribed to the formation of Ti–O–Co bonds. Fig. 4 shows the Ti 2p region, decomposed into two contributions of  $\text{Ti}^{3+}$  ( $457.55 \text{ eV}$  and  $463.30 \text{ eV}$ ) and  $\text{Ti}^{4+}$  ( $458.30 \text{ eV}$  and  $464.05 \text{ eV}$ ) [48,49]. The concentration of  $\text{Ti}^{3+}$  and



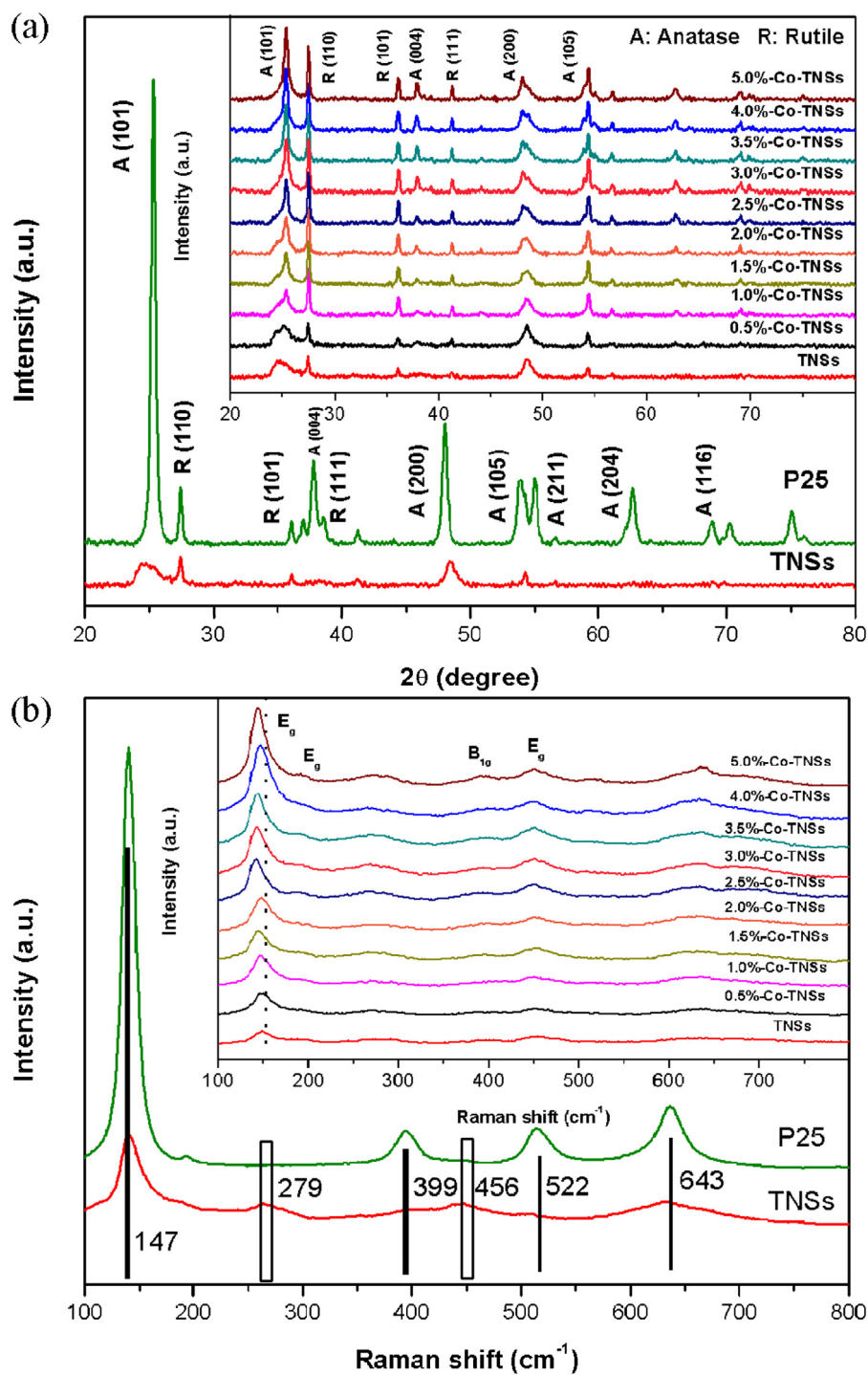


**Fig. 2.** (a) XRD patterns and (b) Raman spectra for P25, TNSs, and x-Co-TNSs (x = 0.0%, 0.5%, 1.0%, 1.5%, 2.0%, 2.5%, 3.0%, 3.5%, 4.0%, and 5.0%).

**Table 2**

The Ti and Co concentration in TNSs, 2.5%-Co-TNSs, 5.0%-Co-TNSs.

	Samples		
	TNSs	2.5%-Co-TNSs	5.0%-Co-TNSs
Ti <sup>3+</sup> concentration (%)	6.31	9.84	10.46
Ti <sup>4+</sup> concentration (%)	93.69	90.16	89.54
Co <sup>2+</sup> concentration (%)	–	34.2	29.8
Co <sup>3+</sup> concentration (%)	–	65.8	70.2

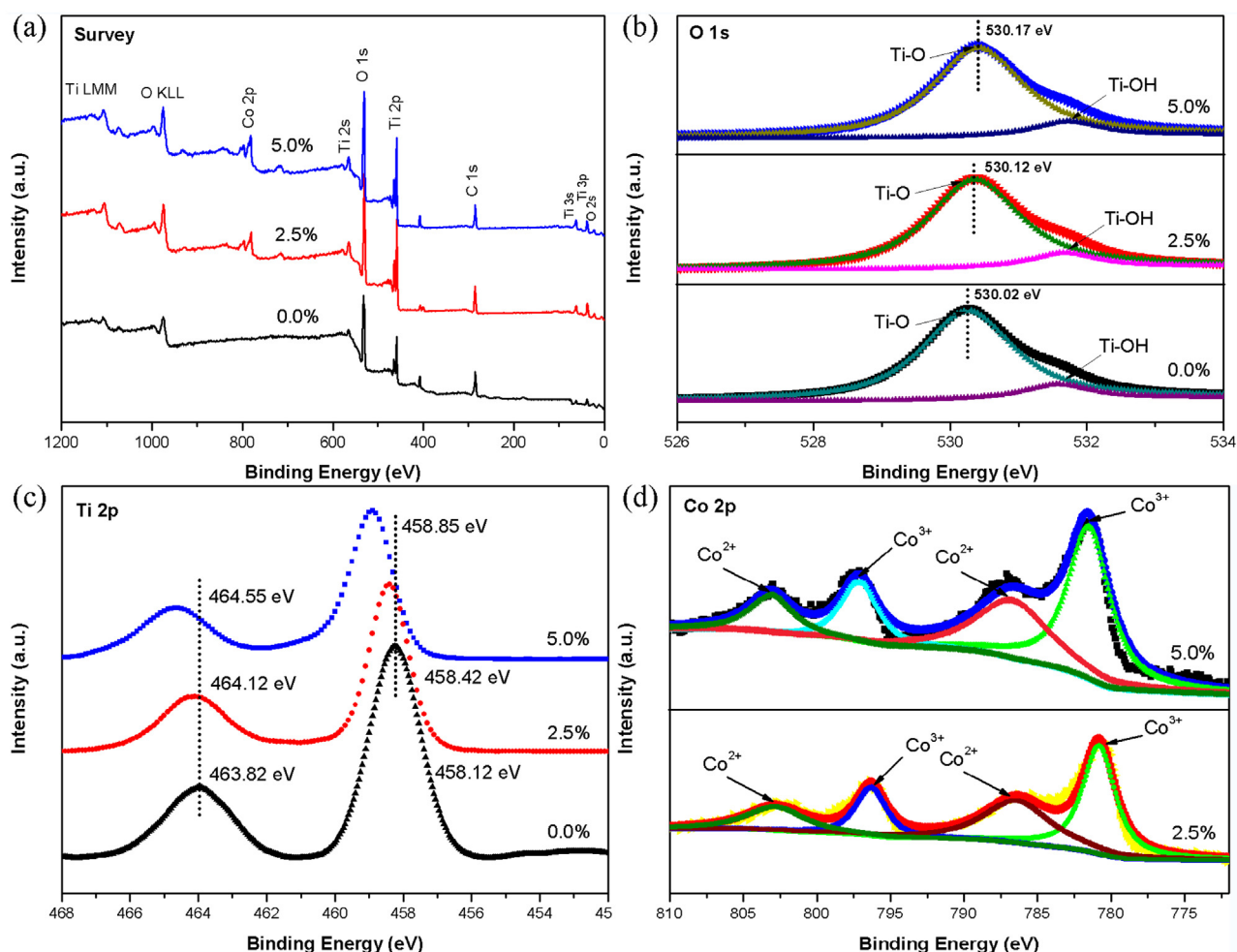


**Fig. 3.** XPS spectra (a) survey spectrum; (b) O1s region of TNSs, 2.5%-Co-TNSs, and 5.0%-Co-TNSs; (c) Ti 2p region of TNSs, 2.5%-Co-TNSs, and 5.0%-Co-TNSs; (d) Co 2p region of 2.5%-Co-TNSs and 5.0%-Co-TNSs.

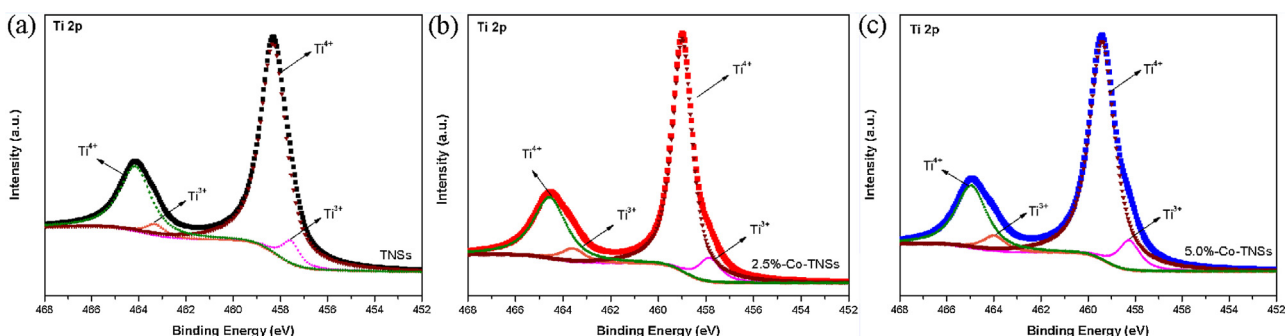


**Fig. 4.** The Ti 2p XPS spectra of samples (a) TNSs, (b) 2.5%-Co-TNSs, (c) 5.0%-Co-TNSs.

Ti<sup>4+</sup> were estimated using the area of their corresponding peaks. It can be found that the concentration of Ti<sup>3+</sup> increases gradually with the loaded amount of CoO<sub>x</sub> (Table 2). And in general, Ti<sup>3+</sup> is considered to be a beneficial state for the photocatalytic performance. It is speculated that the reduction of Ti<sup>4+</sup> takes place in the de-lamination and growth process of Co-TNSs. During the process of hydrothermal reaction, the introduced cobalt will be adsorbed on the surface of raw TiO<sub>2</sub>, and may influence the de-lamination of P25 and the growth of nanosheets. This may be the reason for the reduction of Ti<sup>4+</sup> in the Co-TNSs. Fig. 3d shows the XPS spectra of the Co 2p region. Deconvolution of complex Co 2p spectrum indicates the presence of two chemically distinct species: Co<sup>2+</sup> and

Co<sup>3+</sup>. In particular, two distinct peaks at 781.23 and 796.81 eV could be assigned to 2p<sub>3/2</sub> and 2p<sub>1/2</sub> of Co<sup>3+</sup>, respectively; whereas two small peaks at 786.54 and 803.21 eV could be attributed to 2p<sub>3/2</sub> and 2p<sub>1/2</sub> of Co<sup>2+</sup>, respectively [50,51]. Co 2p<sub>3/2</sub> peak appears at 781.23 eV in 2.5%-Co-TNSs sample, which indicates that the trivalent state of Co ions is dominant. The shifting in the position of Co 2p<sub>3/2</sub> peak to 781.23 eV in 5.0%-Co-TNSs sample indicates the change of a trivalent state of Co ions. The broadening and shifting to the higher binding energy of Co 2p<sub>3/2</sub> could be inferred from the charge transfer between Co<sup>2+</sup> and Co<sup>3+</sup> ions. Using the area of the peak, the content of Co<sup>2+</sup> and Co<sup>3+</sup> has been estimated. It can be found that the introduced cobalt gives rise to the increase of Co<sup>3+</sup>.



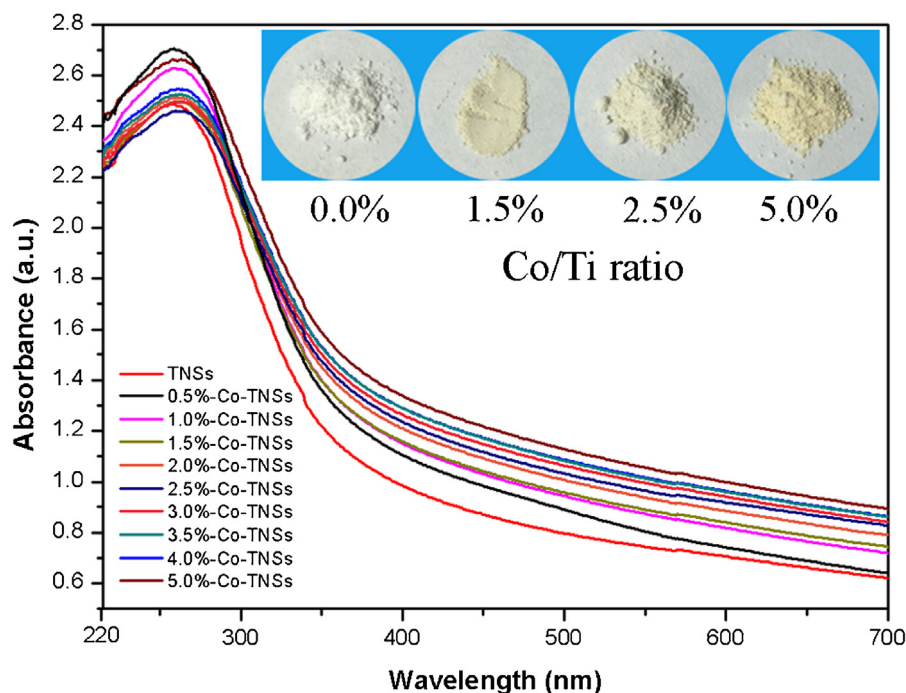


Fig. 5. UV-vis diffuse reflectance spectra and corresponding colors (insert) of as-prepared bare TNSs, and  $\text{CoO}_x$ -loaded TNSs with a varying Co/Ti molar ratio.

The values of  $\text{Co}^{2+}/\text{Co}^{3+}$  decrease from 51.98% (2.5%-Co-TNSs) to 42.45% (5.0%-Co-TNSs).

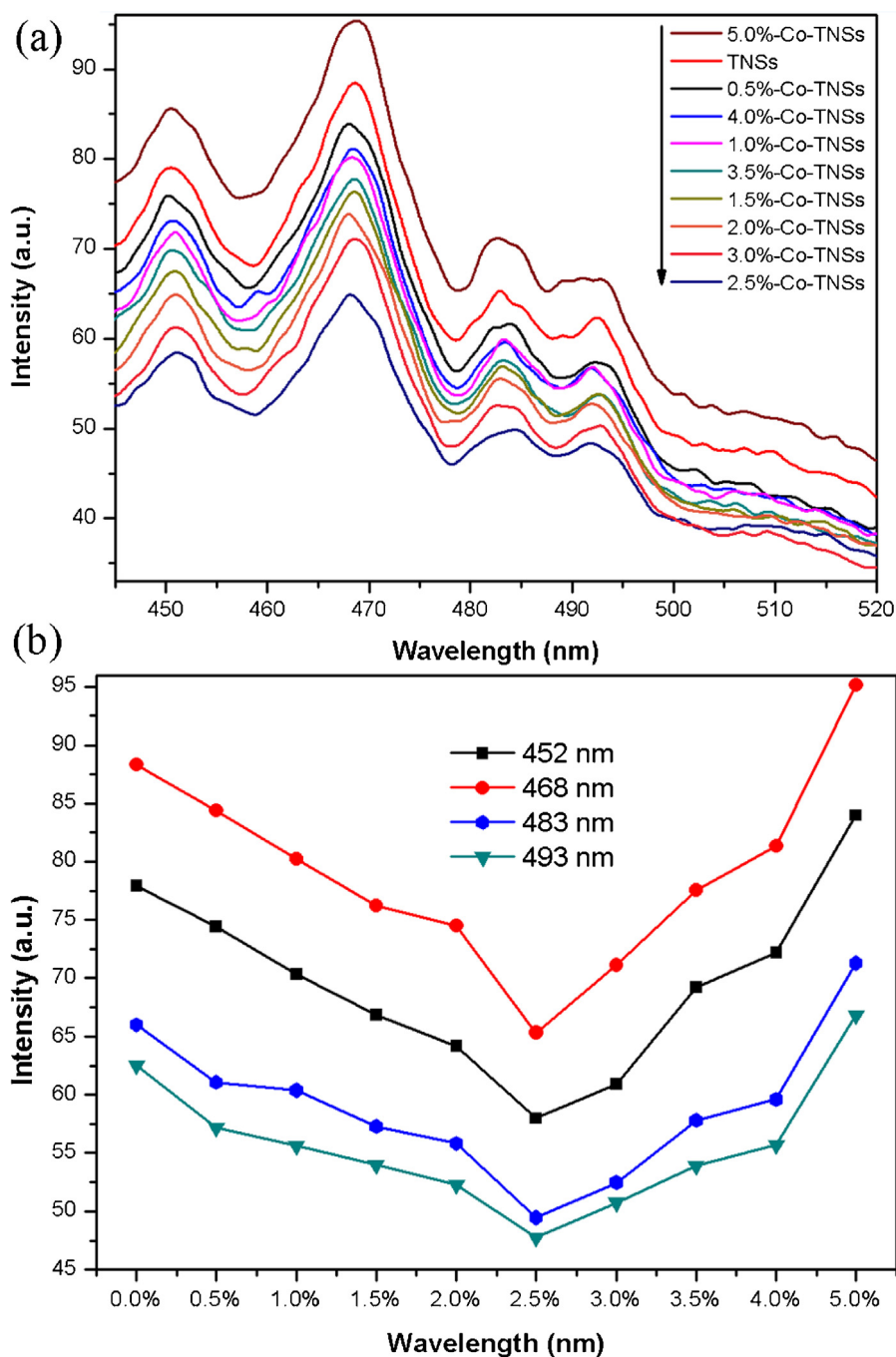
### 3.2. Photoelectric behavior of the pure TNSs and $\text{CoO}_x$ -loaded TNSs photocatalyst

Fig. 5 shows the UV-vis diffuse reflectance spectra and corresponding colors of as-synthesized TNSs and  $\text{CoO}_x$ -loaded TNSs of various Co/Ti molar ratios. As shown in Fig. 5, it can be observed that the optical absorption increased gradually in the VL region with the loaded amount of  $\text{CoO}_x$  nanoparticles, which can be attributed to the absorption of  $\text{CoO}_x$  nanoparticles on the surface of the TNSs. The variation in the color of the photocatalysts intuitively reflects the variation of their optical absorption properties: the samples turn from white to faint yellow and then into grey with increasing the amount of  $\text{CoO}_x$  nanoparticles (the insert of Fig. 5). A red shift appears in the absorption spectra of samples loaded with  $\text{CoO}_x$  at 0.0 at.% and 5.0 at.%. A maximum of the optical absorption is found at 5.0%-Co-TNSs. These results may be attributed to the charge transfer between 3d electrons of Co ion and the conduction (or valence) band  $\text{TiO}_2$ -based nanosheets. Using the Kubelka-Munk function, the absorption data are fitted to equation  $(\alpha h\nu)^{1/2} = A(h\nu - E_g)$  for indirect band-gap transitions, where  $\alpha$  is the absorption coefficient,  $h\nu$ , photon energy,  $E_g$ , the band gap and  $A$  is constant [52]. The band-gap of samples was estimated from the x-intercept of the tangents, and the values are listed in Table 1. With the Co/Ti ratio increasing from 0.0 at.% to 5.0 at.%, the band-gap of specimens receives obvious modulation, reducing from 3.21 eV to 2.90 eV. The photo response becomes stronger gradually with the loaded amount of  $\text{CoO}_x$  nanoparticles. This suggests that the Co-TNSs may release more photo-generated electron-hole pairs than bare TNSs under the same irradiation, thus improve photocatalytic activity in the VL region.

In order to study the possibility of recombination for photo-generated electron-hole pairs, the fluorescence (FL) spectra measurement was carried out for bare TNSs and Co-TNSs samples. The excitation wavelength of the FL measurements was 300 nm

at room temperature. It is well-known that lower recombination seems to be a suggestion of less recombination possibility of photogenerated electron-hole pairs, which facilitates the charge separation process [53]. Fig. 6 shows the FL spectroscopy of bare TNSs and x-Co-TNSs ( $x = 0.0, 0.5, 1.0, 1.5, 2.0, 2.5, 3.0, 3.5, 4.0, 5.0$ ). As FL emission mainly results from the recombination of excited electron-hole pairs, a lower FL intensity indicates a lower recombination rate of electron-hole pairs under the same test conditions. From Fig. 6, it can be seen that four characteristic peaks at 451 nm, 468 nm, 483 nm, and 493 nm appear in the FL spectra. These four FL signals are due to excitonic FL, which mainly result from surface oxygen vacancies and defects of the samples. The FL peaks at 451 and 468 nm are attributed to band edge free exactions, and other two peaks at 483 and 493 nm are attributed to bound excitons [29,53]. The suppression of FL intensity is obtained with the loaded amount of  $\text{CoO}_x$  nanoparticles, demonstrating that  $\text{CoO}_x$  nanoparticles located on surface may act as electron-trapped agents and thus promote electron separation and transfer effects. In addition, it can be found that a small dosage of  $\text{CoO}_x$  ( $\leq 2.5$  at.%) loading can decrease the fluorescence intensity. However, with the loaded amount as high as 5.0 at.%, the sample's fluorescence intensity can be greater than bare TNSs. 2.5%-Co-TNSs showed the minimum efficiency of recombination of photo-generated electron-hole pairs. It can be explained as the result of the excessive loading acted as the recombination centre of electron-hole pairs.

Photo electrochemical properties can be performed by surface photocurrent (SPC) experiment to investigate the separation efficiency of photo-generated electron-hole pairs for photocatalysts. When the experimental conditions are in consistence, higher SPC intensity represents higher separation efficiency of photo-generated electron-hole pairs, suggesting more outstanding capacity of photocatalytic activity [54]. Fig. 7a presents the photo electrochemical responses curves of x-Co-TNSs ( $x = 0.0, 0.5, 1.5, 2.5, 3.5, 5.0$ ) under VL irradiation. As shown in Fig. 7a, the SPC intensities of all samples significantly increased and reach saturation under VL irradiation. With the loaded amount



**Fig. 6.** (a) Fluorescence spectra of as-prepared TNSs and CoO<sub>x</sub>-loaded TNSs using excitation of 300 nm; (b) fluorescence intensity at 452 nm, 468 nm, 483 nm, and 493 nm as a function of loaded amount.

of CoO<sub>x</sub> nanoparticles increasing, the SPC values of Co-TNSs samples increase initially and then decrease. When the loaded amount of CoO<sub>x</sub> is at 2.5 at.%, the SPC values reach maximum. It is obvious that the SPC values of 2.5% Co-TNSs is up to 0.321  $\mu$ A, which is as high as 6.83-fold of that of bare TNSs (0.047  $\mu$ A), representing the highest separation efficiency of photo-generated electron-hole pairs. Conversely, the SPC value of 5.0%-Co-TNSs is lower than that of bare TNSs, indicating that the excess CoO<sub>x</sub> loading would develop recombination centers for the photo-generated electron-hole pairs and thus suppress the separation of photo-generated electron-hole pairs. These results were consistent with the results of FL spectra.

The electrochemical impedance spectroscopy (EIS) was used to investigate the rate of migration of interfacial charges in the samples. Fig. 7b shows the EIS of pure TNSs and x-Co-TNSs ( $x=0.5\%$ , 1.5%, 2.0%, 2.5%, 3.0%, 3.5%, and 5.0%) under VL irradiation. From Fig. 7b, it can be seen that a small amount of CoO<sub>x</sub> loading ( $\leq 2.5$  at.%) leads to a dramatic decrease in the radius of the arc, suggesting that a more effective separation of photo-generated electron-hole pairs [47]. Furthermore, 2.5%-Co-TNSs exhibit the smallest semicircle arc, indicating that a faster interfacial charge transfer in the sample compared to the pure TNSs. Thus, the recombination rate between electrons and holes can be efficiently obstructed, and its photocatalytic ability is significantly improved. In addition, it is noted that

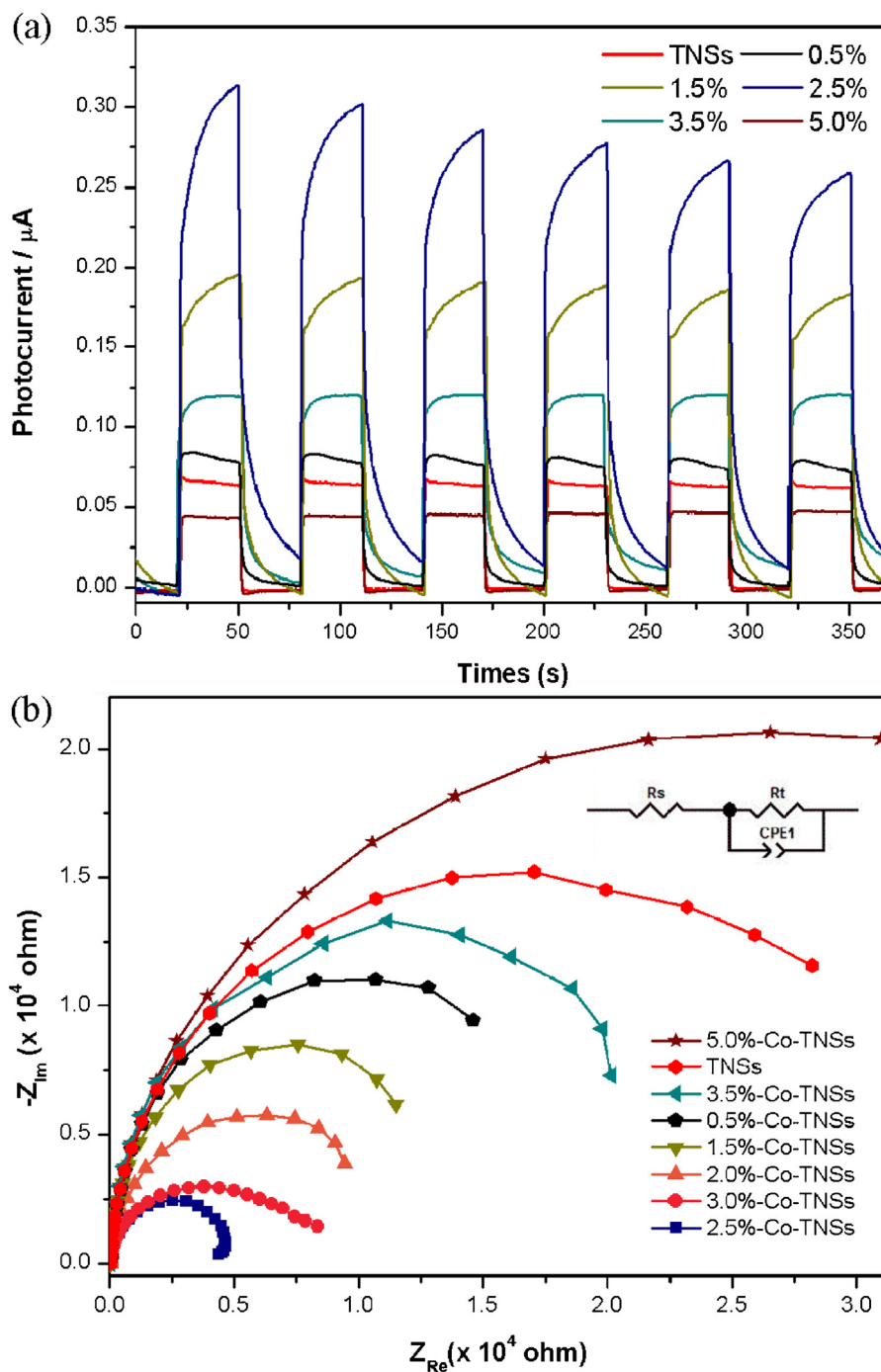


**Fig. 7.** (a) Surface photocurrent curves of bare TNSs, and x-Co-TNSs ( $x = 0.5\%$ ,  $1.5\%$ ,  $2.5\%$ ,  $3.5\%$ , and  $5.0\%$ ); (b) electrochemical impedance spectroscopy of bare TNSs and x-Co-TNSs ( $x = 0.5\%$ ,  $1.5\%$ ,  $2.0\%$ ,  $2.5\%$ ,  $3.0\%$ ,  $3.5\%$ , and  $5.0\%$ ).

the semicircle arc of x-Co-TNSs ( $x \geq 2.5$  at.%) is bigger than that of 2.5%-Co-TNSs, demonstrating that the electron transfer decreased in the high loading amount of samples. Therefore, the appropriate loaded amounts of  $\text{CoO}_x$  nanoparticles ( $x \leq 2.5$  at.%) are beneficial for the transformation of photo-generated charges on the interface of the Co-TNSs composites, and at high amounts of  $\text{CoO}_x$  nanoparticles the photo-generated charges are more likely to recombine at the inter-granular boundaries of the  $\text{CoO}_x$  nanoparticles. Accordingly, the synthesized route gives rise to a good interaction state between TNSs and  $\text{CoO}_x$  nanoparticles, and the formed architecture results in an effective charge separation and transfer

in the interfacial areas. According the analysis results above, it can be found that appropriate loaded amount (2.5 at.%) was considered to be the key reasons for transfer rate of photo-generated charges, suggesting high photocatalytic activity.

### 3.3. Photocatalytic activity evaluation

#### 3.3.1. Photocatalytic effect of pH and $\text{CoO}_x$ -loaded amount in single Cr(VI) solution

The photocatalytic reduction of Cr(VI) in  $\text{K}_2\text{Cr}_2\text{O}_7$  aqueous solution was employed as toxic heavy metals' pollutions to evaluate the

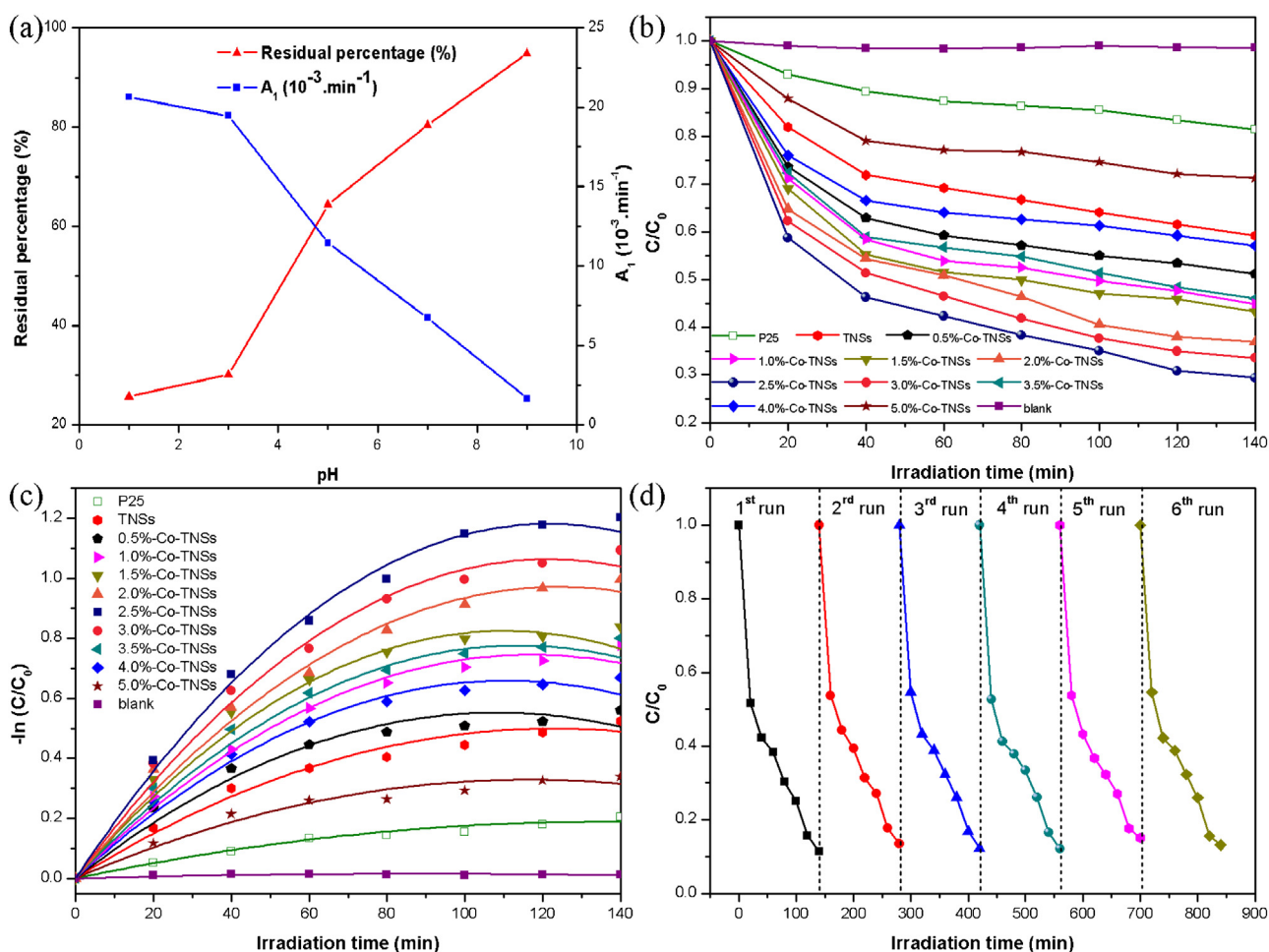
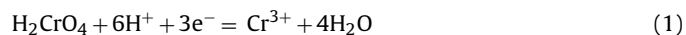
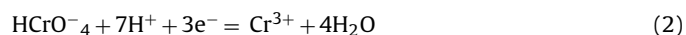


**Fig. 8.** (a) Removal efficiency and degradation rate of Cr(VI) at various pH for 2.5%-Co-TNSs; (b) photocatalytic reduction of Cr(VI) of various samples at pH = 3 under VL irradiation; (c) VL reaction kinetics of Cr(VI) reduction of various samples at pH = 3; (d) reusability of 2.5%-Co-TNSs for the cyclic degradation with initial concentration of Cr(VI) was at 30 ppm, and solution pH was 3.

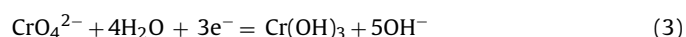
photocatalytic activity of P25, TNSs, and x-Co-TNSs ( $x = 0.5\%$ ,  $1.0\%$ ,  $1.5\%$ ,  $2.0\%$ ,  $2.5\%$ ,  $3.0\%$ ,  $3.5\%$ ,  $4.0\%$ , and  $5.0\%$ ) under VL irradiation. It is well known that photocatalytic reduction of Cr(VI) primarily depend on pH values [56,57]. Fig. 8a shows photocatalytic reduction of Cr(VI) at different pH for 2.5%-Co-TNSs and the reaction rate under VL irradiation. It can be found that the decrease of pH would strongly promote photocatalytic reduction of Cr(VI), and the maximum reaction rate reached  $8.23 \times 10^{-3} \text{ min}^{-1}$  at pH = 1. However, for the pH value 9, the reaction rate was  $0.67 \times 10^{-3} \text{ min}^{-1}$ . Low pH values are attributed to the main species Cr(VI) of  $\text{H}_2\text{Cr}_2\text{O}_7$ , and photocatalytic reaction of Cr(VI) occurred in following way [56–58]:



or



As for alkaline medium, Cr(VI) mainly existed in the form of  $\text{CrO}_4^{2-}$ , and the reaction proceeded as:



It was apparent that the acid medium is beneficial to the photocatalytic reduction of Cr(VI) owing to the existence of abundant  $\text{H}^+$ . Hence, higher efficiency of Cr(VI) would be expected at lower pH. Besides, the photocatalytic efficiency and degradation rate at pH = 1

and pH = 3 were of little difference. Therefore, various  $\text{CoO}_x$ -loaded TNSs were evaluated at pH = 3.

It should be stressed that adsorption capacity of Cr(VI) on the 2.5%-Co-TNSs was as large as 9.18% at pH = 3 as shown in Fig. S4, which is attributed to the enhancement of positively charged nanomaterial at low pH to the adsorption of Cr(VI) electrostatic interaction. However, adsorption of cations onto bare TNSs was minor at low pH due to its low point of zero charge. Fig. 8b and c demonstrates the photocatalytic reduction of Cr(VI) and the reaction kinetic equation over P25, TNSs, and x-Co-TNSs ( $x = 0.5\%$ ,  $1.0\%$ ,  $1.5\%$ ,  $2.0\%$ ,  $2.5\%$ ,  $3.0\%$ ,  $3.5\%$ ,  $4.0\%$ , and  $5.0\%$ ) samples at pH = 3 under VL irradiation. For comparison, blank experiment without adding any photocatalyst is also tested in the same way. The Cr(VI) concentration in blank experiment almost keeps constant, demonstrating that  $\text{K}_2\text{Cr}_2\text{O}_7$  are relatively stable and photolysis reaction is negligible. In addition, after being exposed to VL irradiation for 140 min, there was no observable decrease in Cr(VI) amount for P25 and TNSs, denoting that the P25 and bare TNSs have almost any VL photocatalytic activity for Cr(VI). Conversely, it can be found that x-Co-TNSs ( $x = 0.5\%$ ,  $1.0\%$ ,  $1.5\%$ ,  $2.0\%$ ,  $2.5\%$ ,  $3.0\%$ ,  $3.5\%$ , and  $4.0\%$ ) have higher photocatalytic activity than that of bare TNSs. It can be deduced that loaded  $\text{CoO}_x$  nanoparticles were beneficial for the photocatalytic reduction of Cr(VI). The VL photocatalytic activity of Co-TNSs were significantly improved with the loaded amount of  $\text{CoO}_x$  nanoparticles and reached to a maximum with the Co/Ti ratio at 2.5 at.%, and then decreases rapidly. Further a kinetic sim-



**Table 3**  
Kinetic equations and removal efficiency of P25, undoped TNSs and Co-TNSs composites.

Samples notation	Phenol <sup>a</sup>	Cr(VI) <sup>b</sup>	
	$-\ln(C_t/C_0) = K_{app}t$	$-\ln(C_t/C_0) = B_2t^2 + A_1t$	
	$K_{app} (10^{-3})$	$B_2 (-10^{-5})$	$A_1 (10^{-3})$
P25	1.57	1.01	2.76
TNSs	8.44	3.32	8.13
0.5%-Co-TNSs	10.87	4.71	10.21
1.0%-Co-TNSs	14.17	5.43	12.72
1.5%-Co-TNSs	15.94	6.79	14.97
2.0%-Co-TNSs	17.22	6.31	15.64
2.5%-Co-TNSs	36.52	8.02	19.47
3.0%-Co-TNSs	21.71	7.21	17.56
3.5%-Co-TNSs	12.48	5.99	13.64
4.0%-Co-TNSs	9.74	5.37	11.91
5.0%-Co-TNSs	5.64	2.42	5.65

<sup>a</sup> The degradation of phenol in single phenol system.

<sup>b</sup> The removal of Cr(VI) in single potassium dichromate solution.

ulation is made and the results show that the reactions obey the second-order relationship ( $-\ln(C_t/C_0) = B_2t^2 + A_1t$ ), where  $B_2$  is the coefficient of second-order,  $A_1$ , the coefficient of first-order,  $C_0$ , the initial concentration of solution,  $t$ , the reaction time and  $C_t$  is the concentration of solution at the reaction time of  $t$ . By the polynomial fitting, the reaction rate values are obtained (Fig. 8c). A comparison of the reaction rate constant ( $A_1$ ) indicates that the photocatalytic degradation rate of 2.5%-Co-TNSs ( $0.01947 \text{ min}^{-1}$ ) is 2.39-fold of that of TNSs ( $0.00813 \text{ min}^{-1}$ ) (Table 3). In addition, the cyclic experiments were also carried out to evaluate the photocatalytic stability of Co-TNSs. As shown in Fig. 8d, the 2.5%-Co-TNSs were chosen as a representative to reduce Cr(VI) solution for six cycles. The degradation percentage of Cr(VI) is still up to 90.5% after the sixth cyclic degradation, indicating that 2.5%-Co-TNSs exhibit a good reusability for photocatalytic reduction of Cr(VI).

### 3.3.2. Photocatalytic effect of various electrolyte in single Cr(VI) solution

Electrolyte effects were examined with NaCl, CaCl<sub>2</sub> and Na<sub>2</sub>SO<sub>4</sub> at 5 mM, and corresponding efficiency of removal of Cr(VI) is presented in Fig. S5. Comparing with the system without any electrolyte, addition of NaCl would not have any effect on photocatalytic reduction of Cr(VI). The apparent photo-reduction reaction rate of Cr(VI) was  $0.01923 \text{ min}^{-1}$ , which was close to that in the system without electrolyte ( $0.01952 \text{ min}^{-1}$ ). Besides, co-existence of Na<sup>+</sup> did not exhibit significant inhibition on Cr(VI) reduction, which was in accordance with the previous studies [59,60]. However, addition of CaCl<sub>2</sub> greatly promoted photocatalytic reduction of Cr(VI), and reaction rate was apparently increased to  $0.02021 \text{ min}^{-1}$ . This promotion was due to bivalent Ca<sup>2+</sup> with larger ion radius since Ca<sup>2+</sup> could act as an ionic bridge between Cr(VI) anions. Titanium dioxide was positively charged at pH 5 as its  $\text{pH}_{\text{PZC}}$  was about 6.3–6.6, so Cr(VI) anions (mainly  $\text{HCrO}_4^-$  and  $\text{CrO}_4^{2-}$ ) could be firstly adsorbed onto surface of Co-TNSs and then binded with Ca<sup>2+</sup> via electrostatic attraction [56–58,60]. Afterwards, Ca<sup>2+</sup> could further bridge Cr(VI) anions to form a linkage of  $=\text{TiOH}^+-\text{Cr(VI)}-\text{Ca}^{2+}-\text{Cr(VI)} (= \text{TiOH}^+$  represented surface of TNSs), which made full contact of Cr(VI) with TNSs and thus promoted photocatalysis [59–61]. On the other hand, addition of Na<sub>2</sub>SO<sub>4</sub> inhibits photo-reduction of Cr(VI) with reaction rate decreased to  $0.01786 \text{ min}^{-1}$ , primarily due to competitive adsorption of  $\text{SO}_4^{2-}$  with Cr(VI) on TiO<sub>2</sub>. Overall, electrolytes had some influence to some extent on the removal efficiencies of Cr(VI).

### 3.3.3. Photocatalytic effect of simultaneous decontamination of Cr(VI) and phenol in Cr(VI)-phenol coexisted system

In order to study the photocatalytic effect of simultaneous decontamination of Cr(VI) and phenol in Cr(VI)-phenol coexisted system, the photocatalytic degradation of phenol was performed in single phenol system (20 ppm) for comparison. Fig. S7 shows the photocatalytic degradation of various samples at pH=6.0. As shown in Fig. S7, it is obvious that when the amount of CoO<sub>x</sub> is relatively low ( $\leq 2.5 \text{ at.}\%$ ), the VL photocatalytic activities increase gradually with the loaded amount of CoO<sub>x</sub> nanoparticles, and the photocatalytic activity of 2.5%-Co-TNSs reaches maximum, demonstrating that optimal loading ratio of CoO<sub>x</sub> is 2.5 at.%. With further increasing the loaded amount of CoO<sub>x</sub> nanoparticles ( $\geq 2.5 \text{ at.}\%$ ), the photocatalytic activities of samples decrease gradually under VL irradiation. The photocatalytic activity of 5.0%-Co-TNSs is lower than bare TNSs. As shown in Fig. (S7b–c), the experimental data is found to be in accordance with the first-order kinetic equation ( $\ln(C_t/C_0) = -K_{app}t$ ), where  $K_{app}$  is the apparent rate constant,  $C_0$ , the initial concentration of solution,  $t$ , the reaction time and  $C_t$  is the concentration of solution at the reaction time of  $t$  [29,32]. It is found that the reaction rate  $K_{app}$  of 2.5%-Co-TNSs ( $0.0365 \text{ min}^{-1}$ ) is 4.75-fold of that of TNSs ( $0.00844 \text{ min}^{-1}$ ) under VL irradiation. Therefore, it can be noted that appropriate loaded amount of CoO<sub>x</sub> ( $\leq 2.5 \text{ at.}\%$ ) can effectively enhance the photocatalytic activity of samples. When the loaded amount is higher than the optimal value of 2.5 at.%, loaded CoO<sub>x</sub> nanoparticles will become detrimental. The results of photocatalytic activity are in coincidence with that of FL spectra and SPC spectra. In addition, the cyclic experiments were also carried out to evaluate the photocatalytic stability of Co-TNSs in single phenol system. Further, the 2.5%-Co-TNSs were chosen as a representative to degrade solution for six-time cycle as shown in Fig. S7d. The degradation efficiency of phenol is still up to 97.5% after the sixth cyclic degradation, indicating that 2.5%-Co-TNSs exhibit good reusability for phenol degradation.

For the synergistic photocatalytic removal of Cr(VI) and phenol, 2.5%-Co-TNSs were chosen to evaluate using simultaneous photocatalytic decontamination of Cr(VI) and phenol in Cr(VI)-phenol coexisted system under VL irradiation. The degradation profiles of phenol, with an initial concentration of 20 ppm, in the absence and presence of Cr(VI) at 50 ppm is shown in Fig. 9. From Fig. 9a, it can be found that the presence of Cr(VI) leads to an increase in the rate of phenol degradation. The addition of Cr(VI) results in a kinetic constant, during the first 60 min over 1.38-fold as high as that of isolated phenol. Moreover, it can be found that the extent of phenol degradation also increased greatly as a result of Cr(VI) addition. The improvement in the rate and extent of phenol degradation indicates that Cr(VI) is an efficient scavenger of photo-generated electrons. Conversely, when the photocatalyst was absent, there was no significant reaction between Cr(VI) and phenol under homogeneous conditions at pH 3. Theoretically, it has been shown that, in this kind of photochemical process, the number of charges involved in the oxidation and reduction semi-reactions must be equal and therefore one can anticipate that the promoting effect is mutual. In the presence of Cr(VI), the rate of phenol degradation decreased after 60 mins of irradiation, due to the presence of another electron acceptor oxygen, which can compete the electron from phenol with Cr(VI) since the concentration of Cr(VI) decreased sharply. Similarly, the presence of phenol significantly promoted the reduction rate of Cr(VI) as shown in Fig. 9b. The rate of Cr(VI) reduction was found three-fold higher in the presence of phenol than in its absence.

To gain more insight of the photocatalysis process, the total residual Cr ions concentrations in 2.5%-Co-TNSs photocatalyst after treated samples were measured by ICP emission spectrometer (Fig. 9c). For single Cr(VI) system, after 140 min treatment, a 2.36 ppm of residual Cr (VI) ions concentration was measured.

However, for the mixed system after the same treatment time of 140 min, the measured concentration of residual Cr (VI) ions was found to be as low as 0.047 ppm, much lower than the maximum allowable Cr (VI) concentrations of 0.25 ppm for industrial wastewater and 0.05 ppm for drinking water [57,59,60]. Further XPS was used to study the surface absorbing Cr of the samples after photocatalytic reaction in the single and mixed systems as shown in Fig. 10. The broad peak of Cr 2p<sup>3/2</sup> could be fitted to several peaks at different binding energies. Three main peaks centered at 576.25, 576.31, and 578.61 eV are consistent with the published XPS spectra characteristics of oxides or the hydroxide forms of Cr(III) (e.g., Cr(III)<sub>x</sub>O<sub>y</sub> and Cr(OH)<sub>3</sub>), the other two subordinate peaks at 579.53 and 586.01 eV are corresponded to the characteristics binding energy for the adsorbed Cr(VI) [62,63]. The presence of oxide or hydroxide forms of Cr(III) confirms the photocatalytic reduction of Cr(VI). The result also confirm that the synergistic photocatalysis at 2.5%-Co-TNSs is not only capable of simultaneously reducing Cr(VI) and oxidizing phenol, but also has the capability to remove Cr ions via adsorption.

### 3.4. The analysis of photo-generated •OH radicals for samples

Hydroxyl radical (•OH) is considered to be the most important active groups in photocatalytic reaction. Therefore, in order to realize the impact of CoO<sub>x</sub> loaded TNSs, intensities of 7-hydroxycoumarin fluorescence that changes over time were detected to compare the hydroxyl radical generation rate of different samples. Fig. 11 shows the fluorescence intensities of P25, bare TNSs, and x-Co-TNSs (x = 0.5%, 1.0%, 1.5%, 2.0%, 2.5%, 3.0%, 3.5%, 4.0%, and 5.0%) versus time at 450 nm and the rate constants of formation of 7-hydroxycoumarin of different samples. It is well known that the intensity of fluorescence is proportional to the amount of light generated hydroxyl radicals and the increase of which implies the enhancement of photocatalytic efficiency [64,65]. The PL spectra clearly demonstrated the lower fluorescence intensity of P25 and bare TNSs. As shown in Fig. 11b, with the loaded amount of CoO<sub>x</sub> nanoparticles, there is a remarkable enhancement in the intensity of fluorescence, and then decrease. When the loaded amount of CoO<sub>x</sub> is above 2.5 at.%, which is in accordance with the results of the photocatalytic activity, representing that appropriate amount of CoO<sub>x</sub> loading can significantly improve the rate of formation of hydroxyl radicals, and further implying 2.5 at.% is the optimal loading ratio. The •OH generation rate of 2.5%-Co-TNS is 9.57-fold and 5.21-fold of P25 and undoped TNSs, respectively.

### 3.5. The mechanism for the enhanced photocatalytic activity of CoO<sub>x</sub> loaded samples

To explain the changes in photocatalytic activity under VL irradiation, the excitation and transfer process of charges between CoO<sub>x</sub> and TiO<sub>2</sub>-based nanosheets is schematically illustrated in Scheme 2. The better photocatalytic activity is mainly attributed to the formation of micro-heterostructure between TiO<sub>2</sub>-based nanosheets and CoO<sub>x</sub> nanoparticles. The separation and transfer of charges of the photocatalysts for CoO<sub>x</sub>-loaded TNSs were proposed in the alone Cr(VI) system, and simultaneous decontamination of phenol and Cr(VI) in Cr(VI)-phenol coexisted system under VL irradiation. CoO<sub>x</sub> nanoparticles can be excited to produce photo-generated electron-hole pairs, and then followed by electrons injection from excited CoO<sub>x</sub> into the conduction band of TNSs. Thus, the recombination of electron-hole pairs is effectively suppressed. Beside, for the TiO<sub>2</sub> contains mixed phases of anatase and rutile, when the anatase TiO<sub>2</sub> is mixed with an amount of rutile phase, the electrons will transfer from anatase to a lower energy rutile electron trapping site, on account of the smaller band gap of rutile.

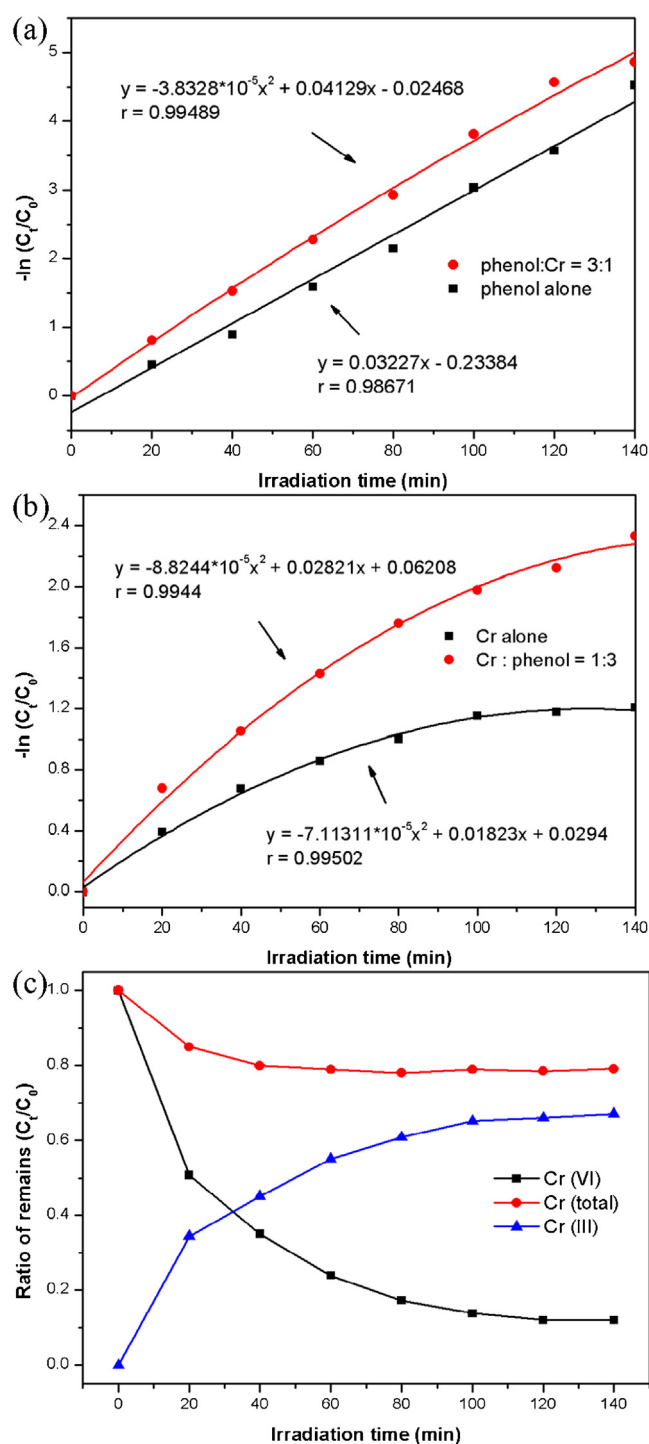


**Fig. 9.** (a) Kinetics of phenol degradation in the absence or present of Cr(VI); (b) the kinetic of Cr(VI) reduction in the absence or present of phenol; (c) removal efficiency of total Cr, Cr(VI), and Cr(III) in Cr(VI)-phenol coexisted system, respectively. Initial concentration of Cr(VI) and phenol were at 50 ppm and at 20 ppm, dosage of 2.5%-Co-TNSs was 1 g L<sup>-1</sup>, solution pH was 3.

The charge separation and transfer of the CoO<sub>x</sub>-loaded TNSs in the process of reduction of Cr(VI) in Cr(VI) system under visible-light irradiation is shown in Scheme 2. For the removal of Cr(VI) in reaction systems, firstly, CoO<sub>x</sub> nanoparticles were excited by VL irradiation, to produce photo-generated electron-hole pairs, followed by electrons injection from excited CoO<sub>x</sub> into the conduction band of TNSs [Eqs. (4)–(5)]. Then absorbed Cr(VI) on the sample was reduced to Cr(III) by electrons [Eq. (6)], and H<sub>2</sub>O accepted holes in

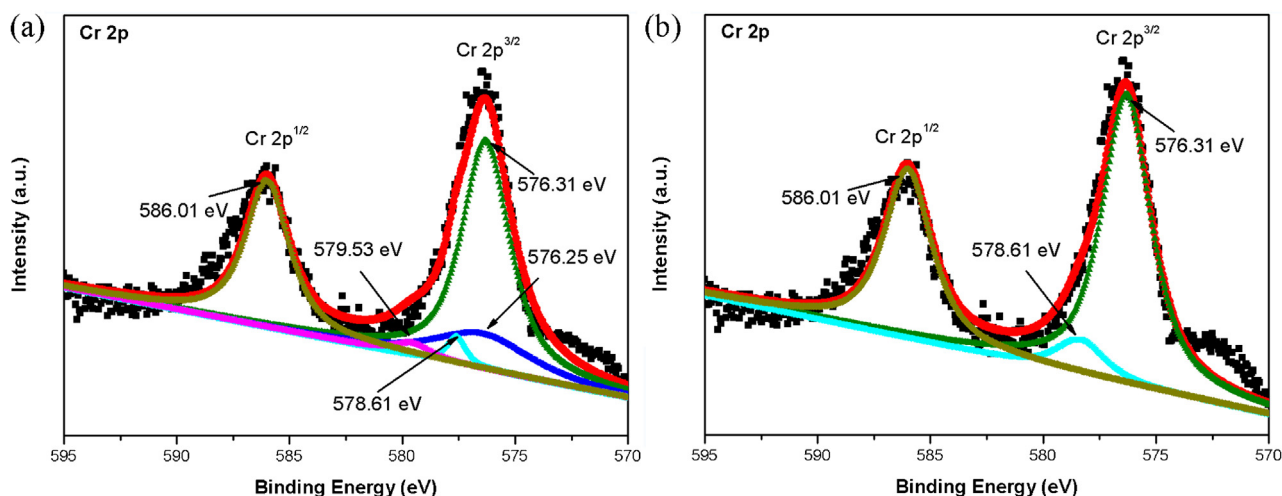


**Fig. 10.** The surface absorbing Cr 2p XPS spectra of the 2.5%-Co-TNSs samples after photocatalytic reaction: (a) in the Cr(VI) single system, (b) in the mixed system of Cr(VI) and phenol.

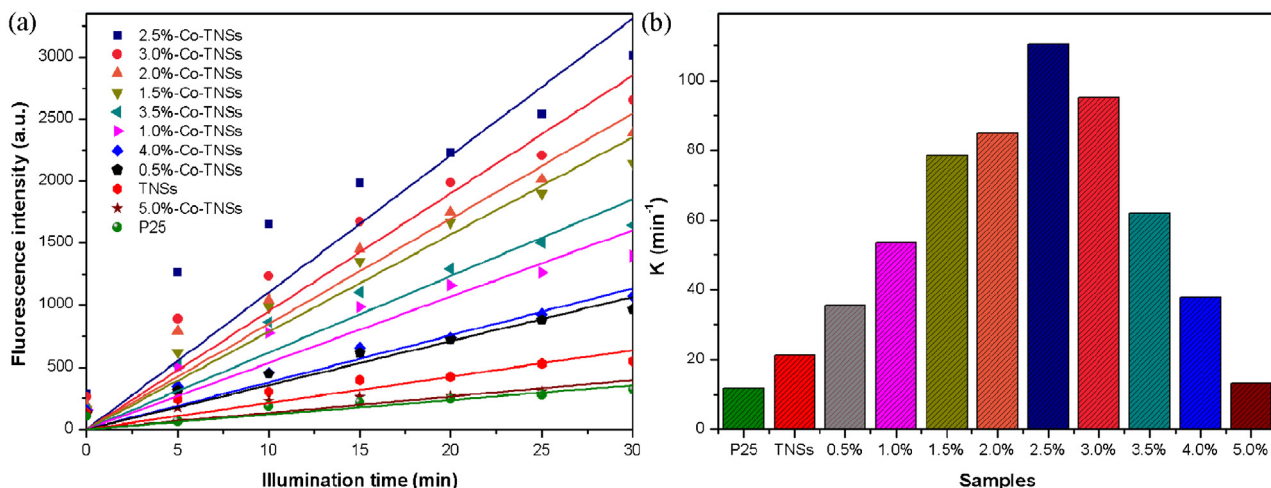


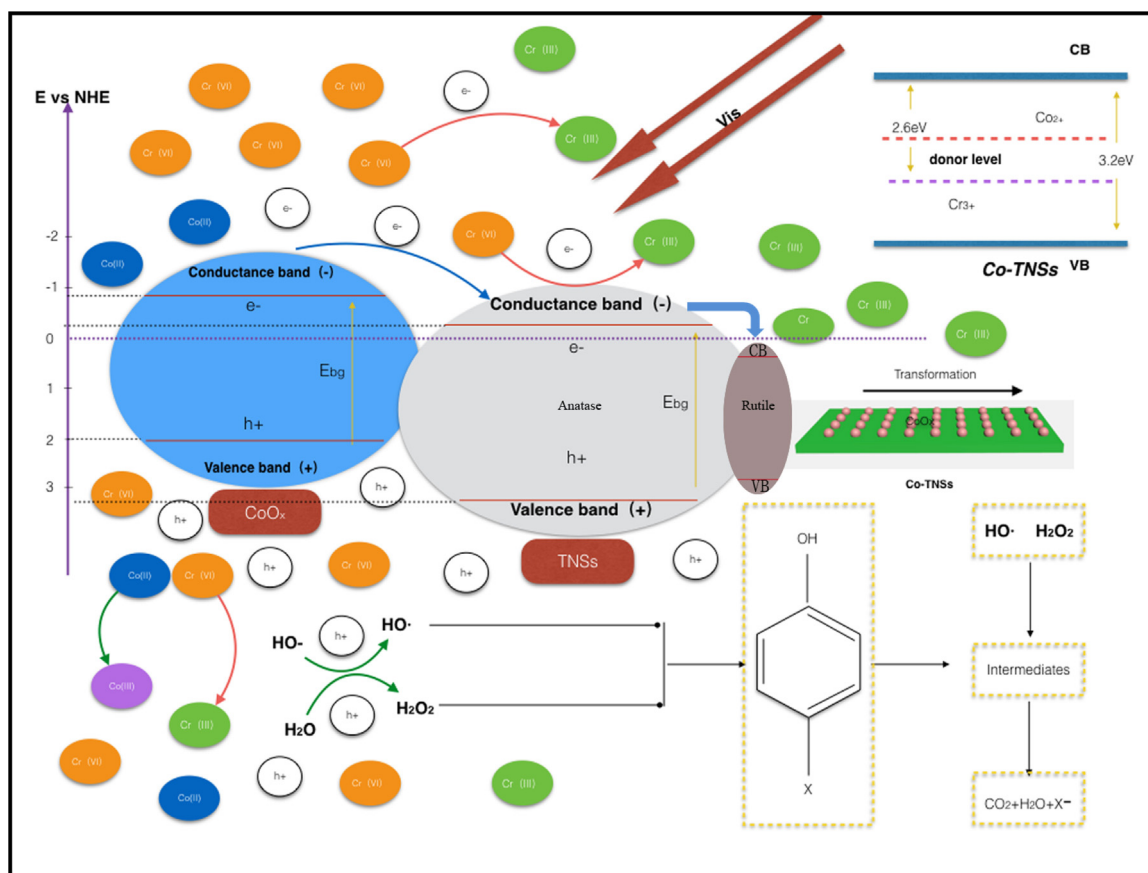
**Fig. 11.** (a) Formation of 7-hydroxycoumarin (monitored by fluorescence emission) in the suspensions of the bare TNSs and CoO<sub>x</sub>-loaded TNSs samples; (b) the formation rate constants of 7-hydroxycoumarin over different samples.

the absence of reducing agents [Eqs. (7)–(10)]. Thereby, the photocatalysis redox cycle continued. In the photocatalysis process, a portion of Cr(VI) would be adsorbed onto CoO<sub>x</sub> nanoparticles by the hydroxyl groups (OH) on the surface. Nevertheless, Cr(III) was mainly adsorbed by TNSs during the adsorption process. Secondly, for CoO<sub>x</sub> loaded TNSs, Cr removal process would be greatly different from that of bare TNSs due to the simultaneous processes, photocatalysis and adsorption taking place. The synergistic effects in this system could be identified in terms of coordination of CoO<sub>x</sub> and TNSs. In the system of both CoO<sub>x</sub> and TNSs, Cr(VI) on the surface of sample was reduced to Cr(III) by photo-induced electrons, and Cr(III) was immediately adsorbed by TNSs owing to their high adsorption capacity and quick kinetics. The transfer of Cr(III) from CoO<sub>x</sub> to TNSs resulted in continuous release of abundant photocatalytic sites of CoO<sub>x</sub> and exposure to Cr(VI), and thus enhanced photocatalytic activity. The close collaboration between CoO<sub>x</sub> and TNSs in the Cr(VI) removal process made it possible to promote photocatalytic reduction of Cr(VI) with ideal receivers of Cr(III) by TNSs adsorption. Thirdly, another aspect need to mention is the role of Cr(III) as an inhibitor. Cr(III) entered into TNSs via ion-exchange with H<sup>+</sup> located in the inner layers of TNSs. The entered Cr(III) could limit the recombination of electrons and holes, thus promoting photocatalytic activity of sample. In addition, when Cr(III)

entered into TNSs at later stage, a donor level (2.6 eV) formed in the forbidden band of TNSs, which would enhance the photocatalytic ability of sample and thus allowed the Co-TNSs-Cr(III) to photo reduce Cr(VI) to certain extent, which is one of the important reasons for synergistic effects [66,67]. The isorbance of Cr(III) not only made UV-vis adsorption spectra of samples increase, but also can effectively improve the separation efficiency of photo-generated charges shown as follows.

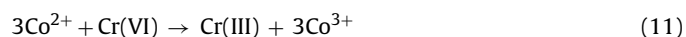
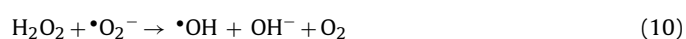
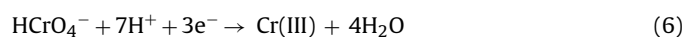
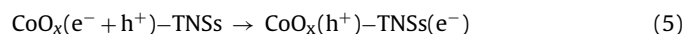
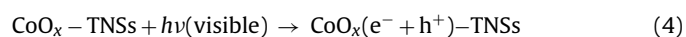
Cr(III) adsorbed 2.5%-Co-TNSs (marked as 2.5%-Co-TNSs-Cr(III)) were then characterized. As shown in diffuse reflectance UV-vis adsorption spectra (Fig. 12a), it can be found that 2.5%-Co-TNSs-Cr(III) showed two absorption bands at ca. 360 and 380 nm, which was ascribed to the intrinsic absorption of Cr(III) [68,69]. Moreover, adsorption of Cr(III) greatly improved the absorption of 2.5%-Co-TNSs in the VL region, with an absorption edge of 478 nm. According to the band gap ( $E_g$ ) formula:  $E_g = 1240/\lambda$ , where  $\lambda$  is the wavelength of the absorption band. The band gap of 2.5%-Co-TNSs and 2.5%-Co-TNSs-Cr(III) was calculated, and was 3.05 eV and 2.61 eV, respectively. So after Cr(III) entered, a donor level (2.61 eV) formed in the forbidden band of 2.5%-Co-TNSs, when Cr(III) in the inter-layers of 2.5%-Co-TNSs captured a photon, the photogenerated electron ( $e^-$ ) from the donor level would transfer to the conductive band of TNSs and leave a hole ( $h^+$ ) behind. Meanwhile, OH<sup>-</sup> in





**Scheme 2.** Schematic diagram for the charge separation and transfer of the photocatalysts for  $\text{CoO}_x$ -loaded TNSs in the process of simultaneous decontamination of  $\text{Cr(VI)}$  and phenol in the  $\text{Cr(VI)}$ -phenol coexisted system under VL irradiation.

the solution acted as  $\text{h}^+$  scavenger, and reacted with  $\text{h}^+$ . So photocatalysis of 2.5%-Co-TNSs-Cr(III) was enhanced due to the efficient separation of the photo-generated electron-hole pairs when the donor level formed. Fig. 12b shows fluorescence spectra of 2.5%-Co-TNSs and 2.5%-Co-TNSs-Cr(III). It could be observed that the two samples exhibited three emission peaks at 400, 451 and 467 nm [29,53,69–71]. The fluorescence spectra peak intensity of 2.5%-Co-TNSs-Cr(III) is much lower than that of 2.5%-Co-TNSs, indicating that the number of recombination sites of electron and hole pairs reduced due to the formation of donor level. The results are further confirmed by the change of surface photocurrent response and nyquist impedance diagrams (Fig. 12c and d).



The characteristic enhancement of synergistically photocatalytic reduction of  $\text{Cr(VI)}$  and oxidation of phenol for 2.5%-Co-TNSs in the  $\text{Cr(VI)}$ -phenol mixed system is schematically illustrated in Scheme 2.  $\text{Cr(VI)}$  as a strong oxidant can rapidly consume photocatalytically generated electrons at the conduction band of samples as

described above, while phenol as an oxidisable organic matter consumes the photocatalytically generated holes (described as follows) at the valence band thereby giving rise to an effective suppression of the charge recombination leading to a dramatic enhancement in photocatalytic activity when compared to the single systems.

At the valence band of TNSs and  $\text{CoO}_x$  nanoparticles,  $\text{O}_2$  captures the reactive electrons that gathered in the conduction band of TNSs to yield  $\bullet\text{OH}$  radical anion and  $\text{H}_2\text{O}_2$  [Eqs. (12)–(15)], and  $\bullet\text{OH}$  radicals can be formed by the reaction between these new intermediates [Eqs. (16)–(17)]. The generation of  $\bullet\text{OH}$  radicals plays a significant role in the photocatalytic reactions, as the  $\bullet\text{OH}$  radicals are key reactive oxygen species in photocatalytic oxidation of phenol molecules. Apart from this, excess holes are left on the irradiated  $\text{CoO}_x$  nanoparticles immediately after the transfer of electrons into the conduction band of TNSs. The oxidation on  $\text{CoO}_x$  nanoparticles may also be due to the direct reaction between photo-generated holes and adsorbed organics (e.g., phenol molecules). As the result, the final products of phenol oxidation,  $\text{CO}_2$  and  $\text{H}_2\text{O}$ , are formed by a series of possible reactions. According to the crystal field theory, due to the half-filled d orbital ( $\text{d}^5$ ),  $\text{Co}^{2+}$  is relatively stable than  $\text{Co}^{3+}$  and  $\text{Co}^+$  ions. Hence, the trapped charges can easily release from  $\text{Co}^+$  or  $\text{Co}^{3+}$  and then transfer to the surface to initiate the photocatalytic reaction.  $\text{Co}^+$  can be oxidized to  $\text{Co}^{2+}$  by transferring electrons to absorbed  $\text{O}_2$  on the surface of sample [Eqs. (19)–(21)]. In the meanwhile, the adsorbed  $\text{O}_2$  is reduced to  $\text{O}_2^{\bullet-}$  [Eqs. (12)], which can further degrade phenol shown in Scheme 2. Similarly,  $\text{Co}^{3+}$  also is reduced to  $\text{Co}^{2+}$ , while surface hydroxyl group translates into hydroxyl radical [Eq. (22)]. Thus, photo-generated superoxide ion ( $\text{O}_2^{\bullet-}$ ) and hydroxyl radical ( $\bullet\text{OH}$ ) are highly reactive when degrade the phenol solution. These processes not only can accelerate the



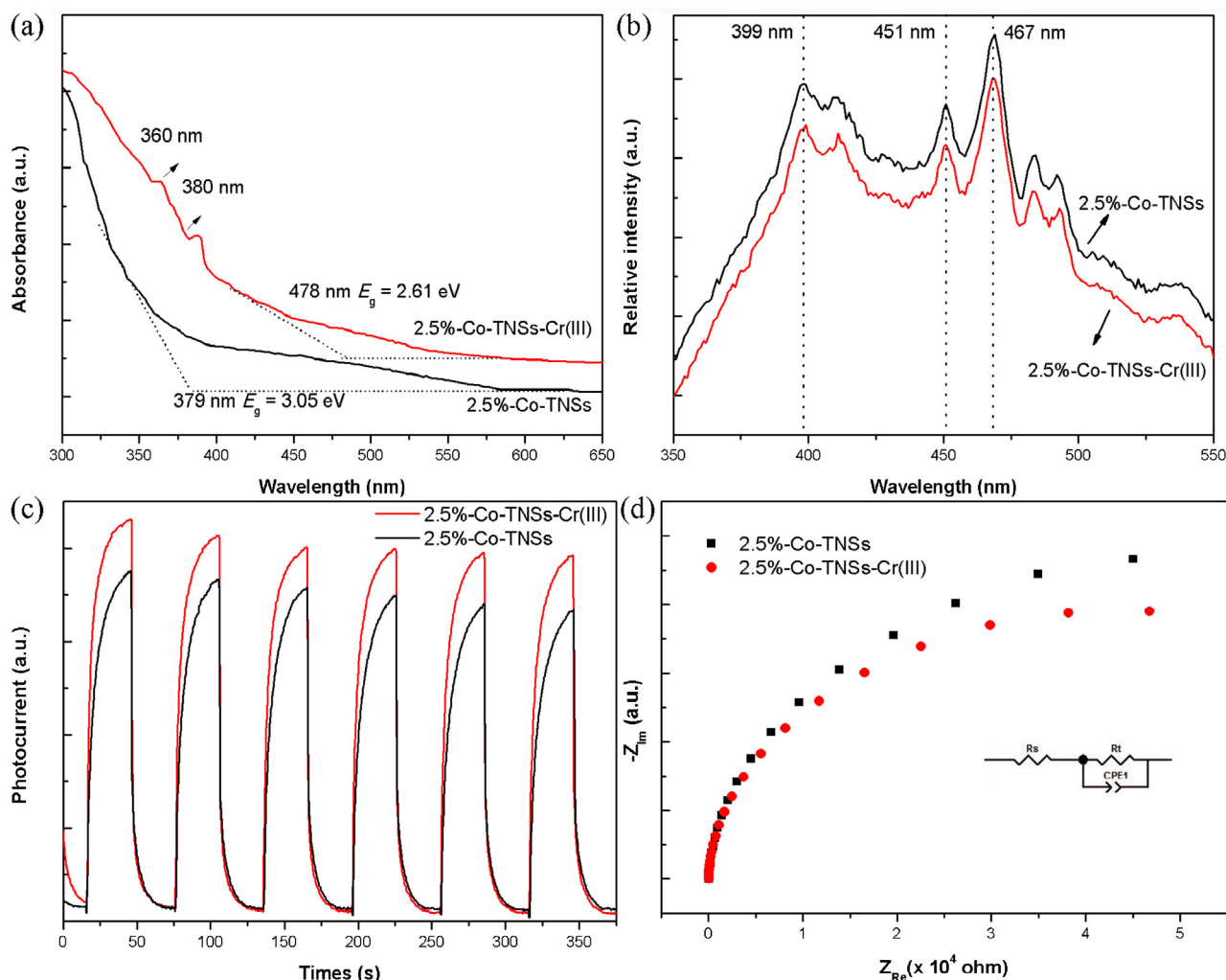
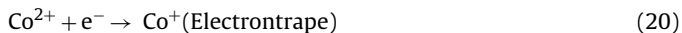
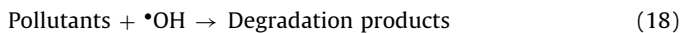
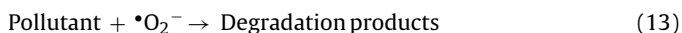
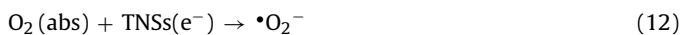


**Fig. 12.** (a) Diffuse reflectance UV-vis adsorption spectra of 2.5%-Co-TNSs and 2.5%-Co-TNSs-Cr(III); (b) fluorescence spectra of 2.5%-Co-TNSs and 2.5%-Co-TNSs-Cr(III) using excitation of 300 nm; (c) photo electrochemical responses curves of 2.5%-Co-TNSs and 2.5%-Co-TNSs-Cr(III); (d) nyquist impedance diagrams 2.5%-Co-TNSs and 2.5%-Co-TNSs-Cr(III).

interfacial charge transfer rate, but also enhance the generation of highly reactive oxidative species such as superoxide and hydroxyl radicals.



Therefore, for the Cr(VI)-phenol mixed system, Cr(VI) as a strong oxidant can rapidly consume photocatalytically generated electrons at the conduction band (CD) of samples, simultaneously

phenol as an oxidisable organic matter consumes the photocatalytically generated holes (described as above) at the valence band (VD) thereby giving rise to an effective suppression of the charge recombination leading to a dramatic enhancement in photocatalytic efficiency when compared to the single systems. Through the consumption of electrons of Cr(VI) at the CD and hole-capture of phenol at VD greatly enhanced the efficiency of separation of photo-generated electron-hole pairs, thus improved the photocatalytic reduction efficiency of Cr(VI) and photocatalytic degradation of phenol.

### 3.6. Regeneration process and reusability efficiency of the whole cycles for CoO<sub>x</sub>-loaded TNSs samples in Cr(VI)-phenol coexisted system

Regeneration and utilization of nanomaterial have a vital role to its widely practical application. 2.5%-Co-TNSs were carried out as a representative to evaluate the structure and photocatalytic activity after regeneration. The 2.5%-Co-TNSs after desorption (2.5%-Co-TNSs-Des) and regeneration (2.5%-Co-TNSs-Reg) process were all reused in Cr(VI)-phenol coexisted system for seven cycles. In particular, after desorption, the materials (2.5%-Co-TNSs-Des) almost maintained as high photocatalytic activity as the raw materials. For instance, the removal efficiency of Cr(VI) was 89.25% after the

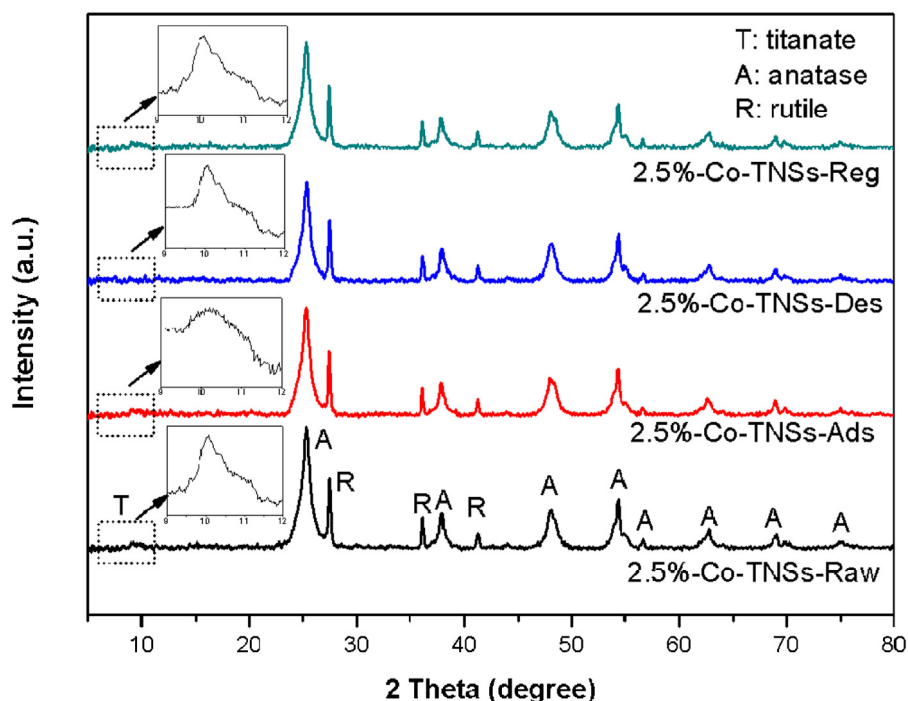


Fig. 13. XRD patterns of series of 2.5%-Co-TNSs samples in the whole cycles.

cycle 1 for 2.5%-Co-TNSs-Reg; the degradation efficiency of phenol (94.75%) only slightly decreased comparing with that of raw materials. The removal efficiency of total Cr(VI) by regenerated materials was as high as 81.57% and the degradation efficiency of phenol was 83.24% even after seven cycles, indicating excellent photocatalytic performances of the materials. Therefore, the regeneration procedure is necessary to recovery of the structure of Co-TNSs, which is essential to maintain high adsorption capability and thus the synergetic efficiency in reuse of nanomaterial.

The nanomaterial (2.5-Co-TNSs-Raw) after adsorption (2.5-Co-TNSs-Ads), desorption (2.5-Co-TNSs-Des) and regeneration (2.5-Co-TNSs-Reg) process were all reused in Cr(VI)-phenol coexisted system for seven cycles. The different-stages structure of samples in the whole cycles were further characterized by XRD, Raman spectra, TEM, HRTEM and XPS. Fig. 13 depicts the XRD patterns of different-stages of 2.5%-Co-TNSs in the whole cycles. All samples were of anatase, rutile, and titanate phase. The peaks at  $2\theta \approx 25^\circ, 37^\circ, 48^\circ, 53^\circ, 55^\circ, 63^\circ, 69^\circ, 71^\circ$  and  $75^\circ$  were all assigned to anatase phase, while the peaks at about  $27^\circ, 36^\circ, 39^\circ$  indicate rutile phase [64,65]. Almost, there is no change of crystal phase for samples in the whole photocatalytic process. Due to the poor crystallinity of the sample, the diffraction peaks of titanate were not well defined. The peak at  $2\theta \approx 10^\circ$  which was ascribed to the interlayer structure of TNSs was chosen as a reference to investigate the change of TNSs structure in the recycle process [72,73]. This peak is slightly weakened after the adsorption of Cr(III), suggesting that the adsorption process was only ion-exchange between Cr(III) and  $H^+$  but would not affect the skeletal structure of titanate. However, the interlayer structure recovered after desorption with  $HNO_3$  as the peak at  $10^\circ$  regained, and thereby increase the adsorption capacity of Cr(III) for 2.5%-Co-Des. After light irradiation treatment in the presence of  $H_2O_2$  solution during regeneration process, the interlayer structure recovered and the 2.5%-Co-Reg reformed for efficient adsorption of Cr(III).

Raman analysis was also carried out to analyze the regeneration of Ti–O (titanate) groups. Fig. 14 shows Raman spectra of 2.5%-Co-TNSs-Raw, 2.5%-Co-TNSs-Ads, 2.5%-Co-TNSs-Des, and

2.5%-Co-TNSs-Reg samples. The spectra of 2.5%-Co-TNSs-Raw were the same as bare TNSs prepared under concentrated NaOH solution and at high temperature (10 M,  $130^\circ C$ ) [74,75]. The peaks at  $279\text{ cm}^{-1}$  and  $456\text{ cm}^{-1}$  were ascribed to Ti–O bending and stretching vibrations involving six-coordinated titanium atoms in the  $[TiO_6]$  octahedron. These peaks hardly changed after the ion-exchange between Cr(III) ions and  $H^+$  (2.5%-Co-TNSs-Ads), indicating the stability of  $[TiO_6]$  skeleton during the adsorption process. After desorption, the peak at around  $456\text{ cm}^{-1}$  shifted to  $449\text{ cm}^{-1}$ , and another satellite peak at  $377\text{ cm}^{-1}$  appeared, which was related to a minor damage of  $TiO_2$ -based nanosheets. After adsorption of Cr(III), a tiny peak at  $827\text{ cm}^{-1}$  corresponding to Ti–O–Cr appeared. Subsequently, the shift to  $449\text{ cm}^{-1}$  of 2.5%-Co-TNSs-Des recover to original position ( $456\text{ cm}^{-1}$ ), and peaks at  $377\text{ cm}^{-1}$  and  $827\text{ cm}^{-1}$  (Ti–O–Cr) disappeared [74,75]. The spectra of 2.5%-Co-TNSs-Reg were almost the same as that of original 2.5%-Co-TNSs-Raw, especially the Ti–O peak at  $279\text{ cm}^{-1}$  and  $456\text{ cm}^{-1}$ , indicating very good regeneration of 2.5%-Co-TNSs.

TEM and HRTEM analysis were conducted to investigate the changes in the different-stage morphology for the 2.5%-Co-TNSs in the whole cycles. Fig. 15 shows the varying morphology of 2.5%-Co-TNSs at different stages including raw status, adsorption, desorption, and regeneration stages. As described in Fig. 15a and b,  $TiO_2$ -based nanosheets were randomly showed in original system, and surface-enriched  $CoO_x$  nanoparticles dispersed on the surface TNSs. The 2.5%-Co-TNSs-Ads after adsorption of Cr(VI) is still of irregular sheet-like polygons (Fig. 15c), and almost no change in the morphology due to the adsorption process. As shown in Fig. 15d the multi-walled structure of nanosheets was not damaged after desorption. The regeneration process after light irradiation by adding  $H_2O_2$  solution would recover original sheet-like structure (Fig. 15e and f). Comparing with the HRTEM of 2.5%-Co-TNSs-Raw and 2.5%-Co-TNSs-Reg, surface-enriched  $CoO_x$  nanoparticles dispersed on the surface of TNSs were almost unchanged. The content of  $CoO_x$  nanoparticles after regeneration was also evaluated by high-resolution XPS as shown in Fig. 16. Comparing the XPS spectra of 2.5%-Co-TNSs-Raw and 2.5%-Co-TNSs-Reg, it can be found

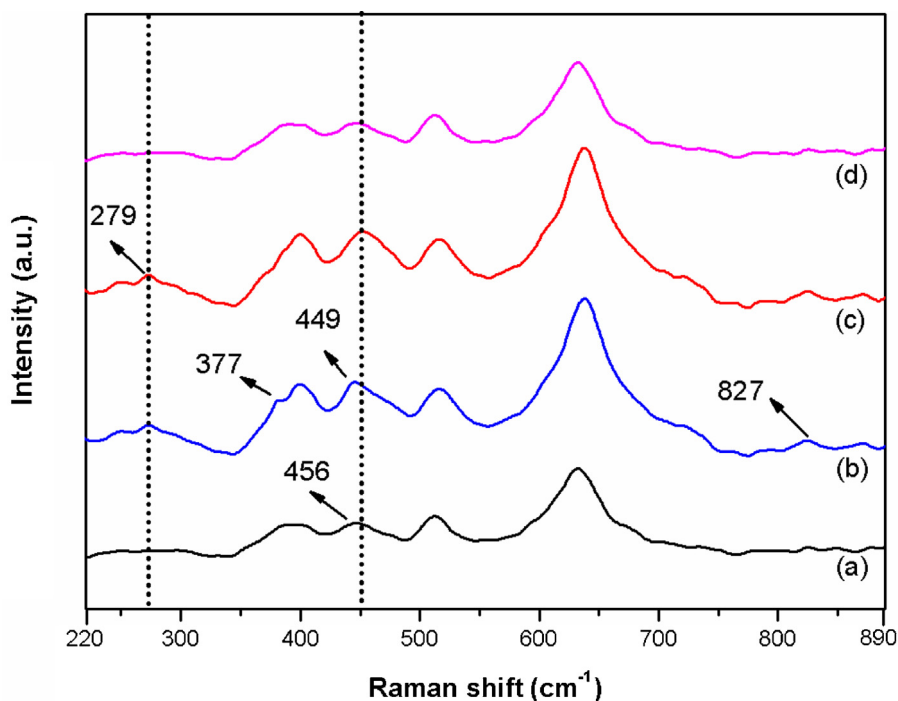


**Fig. 14.** Raman spectra of 2.5%-Co-TNSs and after adsorption, desorption, and regeneration: (a) 2.5%-Co-TNSs-Raw; (b) 2.5%-Co-TNSs-Ads; (c) 2.5%-Co-TNSs-Des; (d) 2.5%-Co-TNSs-Reg.

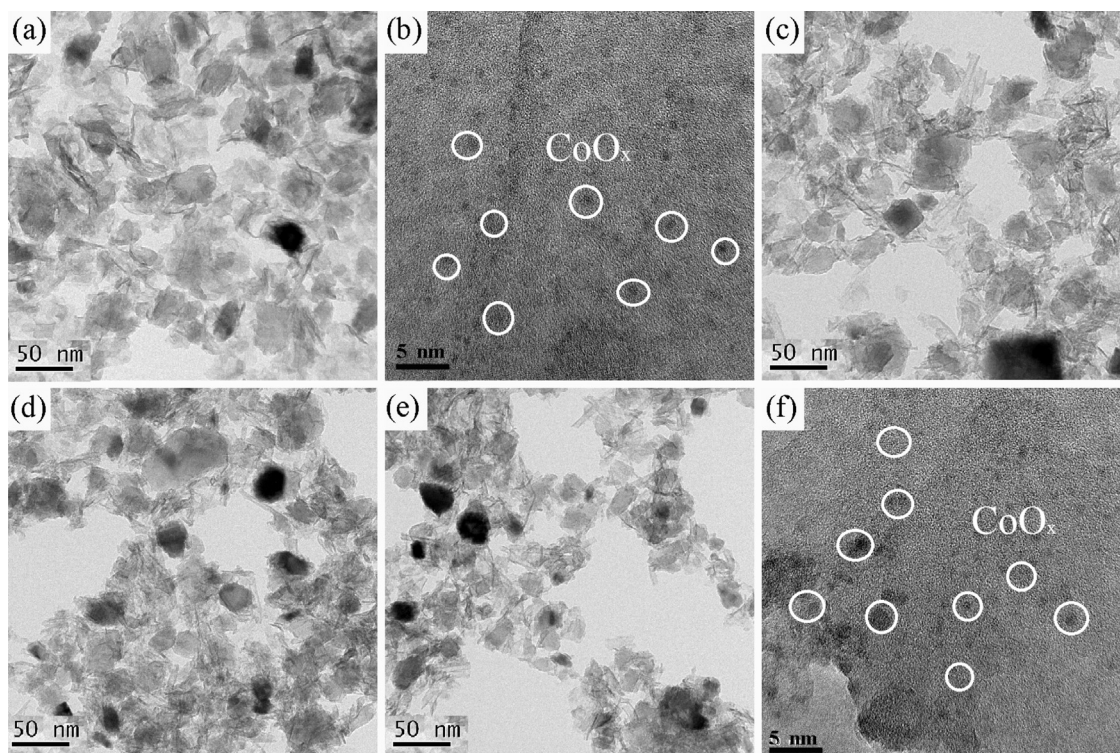


**Fig. 15.** TEM images and HRTEM images of different stages in the whole cycles (a–b) 2.5%-Co-TNSs-Raw, (c) 2.5%-Co-TNSs-Ads, (d) 2.5%-Co-TNSs-Des, (e–f) 2.5%-Co-TNSs-Reg.

that there is almost no difference in the content of  $\text{CoO}_x$  after regeneration (first and seventh cycle), suggesting the structure of as-prepared  $\text{CoO}_x$  loaded TNSs were relatively stable.

The recovery of photocatalysts after usage is of a critical practical issue. In the present study, we found that the Co-TNSs could be

readily separated from aqueous solution via a facile sedimentation process in less than 1 h, while the aqueous suspensions of Degussa P25 powder were still turbid after several hours (Fig. S8, Supporting information). The easy recovery feature makes it possible to reuse the samples. Fig. 17 shows the performance of the recycled



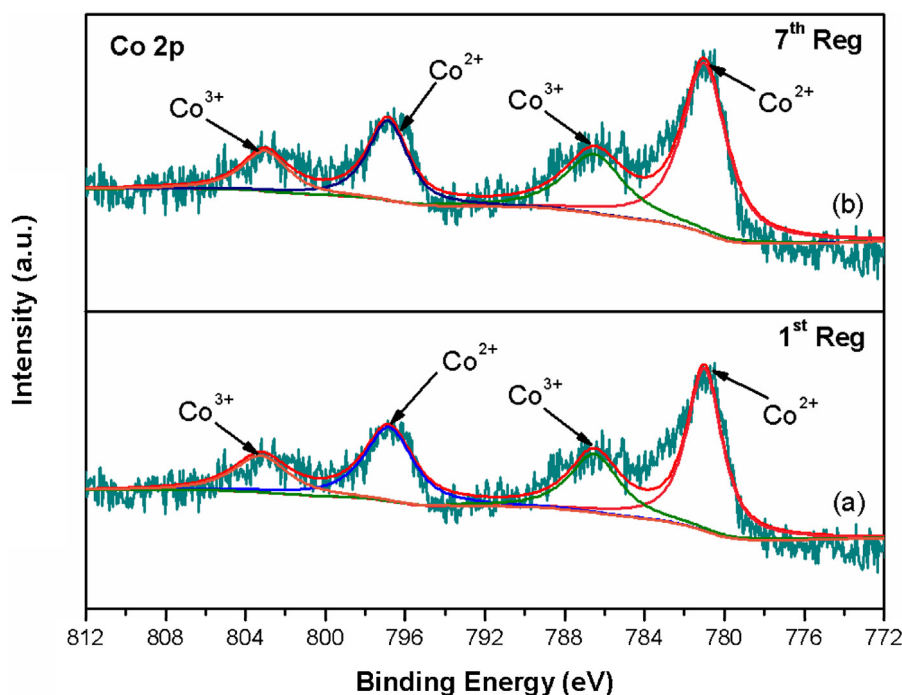


Fig. 16. The Co 2p XPS spectra of samples (a) 2.5%-Co-TNSs after the first regeneration (b) 2.5%-Co-TNSs after the seventh regeneration.

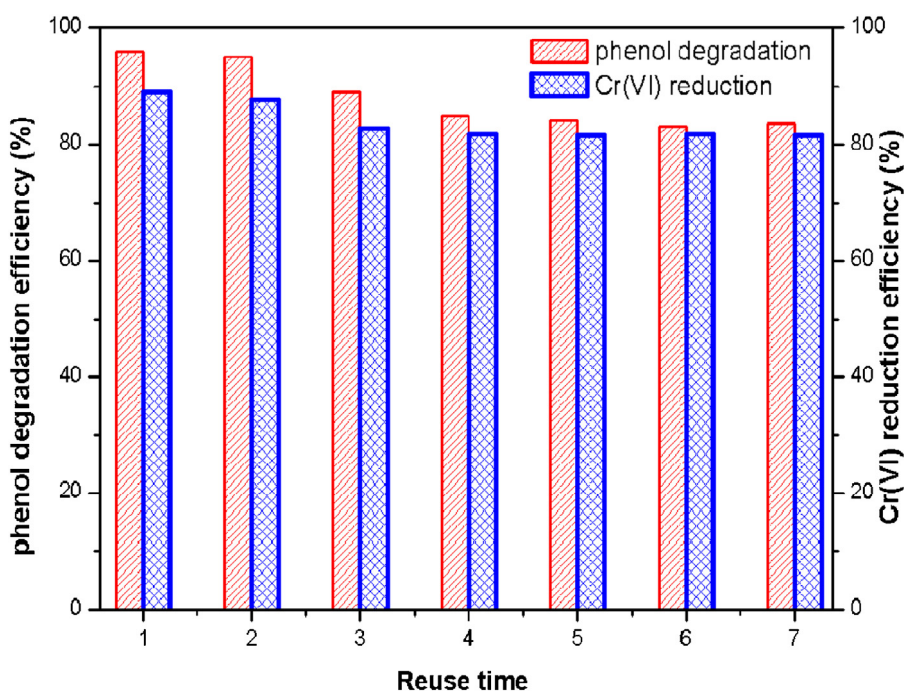


Fig. 17. The reuse of 2.5%-Co-TNSs of Cr(VI) and phenol in Cr(VI)-phenol mixed system.

2.5%-Co-TNSs for the mixed system of Cr(VI) and phenol (210 min under VL irradiation for each cycle). The regenerated 2.5%-Co-TNSs samples (2.5%-Co-TNSs-Reg) were treated by  $\text{HNO}_3$  solution before used to remove the surface-absorbed Cr species, and then irradiated under UV-vis light in the presence of  $\text{H}_2\text{O}_2$  to remove residual phenol. It was found that the Cr(VI) removal efficiency of 2.5%-Co-TNSs was still up to 81.57% after seven cycles, while the removal efficiency of phenol maintained 83.24%. These results

demonstrate a feasibility of recovery and reusability of Co-TNSs samples.

#### 4. Conclusions

$\text{TiO}_2$ -based nanosheets loaded with highly dispersed  $\text{CoO}_x$  ( $\text{Co} = \text{Co}^{2+}, \text{Co}^{3+}$ ) nanoparticles (1–2 nm) were successfully synthesized by a facile one-pot hydrothermal method. The as-synthesized samples show clearly sheet-like structure with the width of



30~100 nm, the length more than 100 nm, higher specific surface area (260–350 m<sup>2</sup>/g), and small thickness (ca. 4 nm), which make TNSs contact with more pollution molecules and effectively improve the transfer rate of photo-generated electron-hole pairs. The structure of these TNSs was influenced dramatically by the loaded CoO<sub>x</sub> nanoparticles. The XRD, BET and Raman spectra indicates that the crystallinity of samples increases gradually with amount of CoO<sub>x</sub>, suggesting a gradual increase in the ratio of TiO<sub>2</sub> during the transformation process from 3D to 2D. XPS results revealed that cobalt mainly exists in the form of Co<sup>2+</sup> and Co<sup>3+</sup>, and the binding energies of Ti–O bonds have been changed with the loading of cobalt oxide. CoO<sub>x</sub> lead a red shift of absorption and band-gap reduced from 3.21 eV to 2.90 eV with the increasing content of CoO<sub>x</sub> from 0.0 at.% to 5.0 at.%. The FL emission intensity initially decreases with the amount of CoO<sub>x</sub>, and then increases after attaining a minimum value at 2.5%-Co-TNSs. FL and SPC indicated loading of appropriate amount of CoO<sub>x</sub> (2.5 at.%) can effectively inhibit the recombination rate of photo-generated electron-hole pairs, thus improve the separation efficiency. The photocatalytic activity was evaluated by removal of Cr(VI) solution under VL irradiation. It can be found that the Co-TNSs photocatalysts showed excellent VL photocatalytic activity for the photocatalytic removal of dichromate Cr(VI) solution. The photocatalytic activity gradually increased with the amount of CoO<sub>x</sub> nanoparticles initially, and then decreased after attaining a maximum value at an optimal content (2.5 at.%) for removal of aqueous Cr(VI) solution. The addition of Ca<sup>2+</sup> could promote photocatalysis owing to its ionic bridging function and form of =TiOH<sup>+</sup>–Cr(VI)–Ca<sup>2+</sup>–Cr(VI) linkages, while SO<sub>4</sub><sup>2–</sup> only slightly inhibited photo-reduction of Cr(VI), indicating good synergy of photocatalysis and adsorption even at high ionic strength of electrolyte. Besides, the photocatalytic reduction of Cr(VI) was significantly promoted by the presence of phenol, and synergism between Cr(VI) reduction and phenol degradation was demonstrated by measuring the effect of repeated use of Co-TNSs on its photocatalytic efficiency. Desorbed Co-TNSs (Co-TNSs-Des) could be easily regenerated and reused for Cr removal with excellent performance. An alternate mechanism for the enhancement of photocatalytic activity under visible light irradiation was also proposed.

## Acknowledgements

This work was financially supported by the National Basic Research Program of China (973 Program, Nos. 2009CB939704, 2009CB939705), the National Natural Science Foundation of China (No. J1210061), Large-scale Instrument and Equipment Sharing Foundation of Wuhan University (No. LF20150582), National Natural Science Foundation of China (No. 51402126), and Natural Science Foundation of Zhejiang Province (No. LQ13B010003).

## Appendix A. Supplementary data

Supplementary data associated with this article can be found, in the online version, at <http://dx.doi.org/10.1016/j.apcatb.2016.03.003>.

## References

- [1] Y.C. Zhang, L. Yao, G. Zhang, D.D. Dionysiou, J. Li, X. Du, *Appl. Catal. B* 144 (2014) 730–738.
- [2] Y.C. Zhang, M. Yang, G. Zhang, D.D. Dionysiou, *Appl. Catal. B* 142–143 (2013) 249–258.
- [3] Y.C. Zhang, J. Li, H.Y. Xu, *Appl. Catal. B* 123–124 (2012) 18–26.
- [4] Y. Zhang, Q. Zhang, Q. Shi, Z. Cai, Z. Yang, *Sep. Purif. Technol.* 142 (2015) 251–257.
- [5] Z.H. Diao, X.R. Xu, F.M. Liu, Y.X. Sun, Z.W. Zhang, K.F. Sun, S.Z. Wang, H. Cheng, *Sep. Purif. Technol.* 154 (2015) 168–175.
- [6] H. Wang, X. Yuan, Y. Wu, G. Zeng, X. Chen, L. Leng, Z. Wu, L. Jiang, H. Li, *J. Hazard. Mater.* 286 (2015) 187–194.
- [7] M.N. Chong, B. Jin, C.W.K. Chow, C. Saint, *Water Res.* 44 (2010) 2997–3027.
- [8] A. Huang, N. Wang, M. Lei, L. Zhu, Y. Zhang, Z. Lin, D. Yin, H. Tang, *Environ. Sci. Technol.* 47 (2013) 518–525.
- [9] C. Pan, Y. Zhu, *Environ. Sci. Technol.* 44 (2010) 5570–5574.
- [10] G. Liu, L. Wang, H.G. Yang, H. Cheng, G.Q. Max Lu, *J. Mater. Chem.* 20 (2010) 831.
- [11] M.R. Hoffmann, S.T. Martin, W. Choi, D.W. Bahnemann, *Chem. Rev.* 95 (1995) 69–96.
- [12] A. Fujishima, T.N. Rao, D.A. Tryk, *J. Photochem. Photobiol. C* 1 (2000) 1–21.
- [13] A.L. Linsebigler, G.Q. Lu, J.T. Yates Jr., *Chem. Rev.* 95 (1995) 735–758.
- [14] Z.Y. Liu, D.D. Sun, P. Guo, J.O. Leckie, *Nano. Lett.* 7 (2007) 1081–1085.
- [15] Y. Lan, X.P. Gao, H.Y. Zhu, Z.F. Zheng, T.Y. Yan, F. Wu, S.P. Ringer, D.Y. Song, *Adv. Funct. Mater.* 15 (2005) 1310–1318.
- [16] S.P. Albu, A. Ghicov, J.M. Macak, R. Hahn, P. Schmuki, *Nano Lett.* 7 (2007) 1286–1289.
- [17] Y. Takezawa, H. Imai, *Small* 2 (2006) 390–393.
- [18] B. Zhao, F. Chen, Q.W. Huang, J.L. Zhang, *Chem. Commun.* 34 (2009) 5115–5117.
- [19] D.V. Bavykin, A.N. Kulak, F.C. Walsh, *Cryst. Growth Des.* 10 (2010) 4421–4427.
- [20] S. Ma, S. Zhan, Y. Jia, Q. Zhou, *ACS Appl. Mater. Int.* 7 (2015) 21875–21883.
- [21] B. Li, Z. Zhao, Q. Zhou, B. Meng, X. Meng, J. Qiu, *Chem. Eur. J.* 20 (2014) 14763–14770.
- [22] U.I. Gaya, A.H. Abdullah, *J. Photochem. Photobiol. C* 9 (2008) 1–12.
- [23] W. Lee, Y. Sung, *Cryst. Growth Des.* 12 (2012) 5792–5795.
- [24] V.N. Kuznetsov, V.K. Ryabchuk, A.V. Emeline, R.V. Mikhaylov, A.V. Rudakova, N. Serpone, *Chem. Mater.* 25 (2013) 170–177.
- [25] H. Choi, Y.J. Kim, R.S. Varma, D.D. Dionysiou, *Chem. Mater.* 18 (2006) 5377–5384.
- [26] J. Yu, L. Qi, M. Jaroniec, *J. Phys. Chem. C* 114 (2010) 13118–13125.
- [27] F. Chen, P. Fang, Y. Gao, Z. Liu, Y. Liu, Y. Dai, *Chem. Eng. J.* 204–206 (2012) 107–113.
- [28] F. Chen, P. Fang, Z. Liu, Y. Gao, Y. Liu, Y. Dai, H. Luo, J. Feng, *J. Mater. Sci.* 48 (2013) 5171–5179.
- [29] D. Lu, P. Fang, X. Liu, S. Zhai, C. Li, X. Zhao, J. Ding, R. Xiong, *Appl. Catal. B* 179 (2015) 558–573.
- [30] D. Lu, B. Zhao, P. Fang, S. Zhai, D. Li, Z. Chen, W. Wu, W. Chai, Y. Wu, N. Qi, *Appl. Surf. Sci.* 359 (2015) 435–448.
- [31] J. Zhu, S. Wang, J. Wang, D. Zhang, H. Li, *Appl. Catal. B* 102 (2011) 120–125.
- [32] R. Qiu, D. Zhang, Z. Diao, X. Huang, C. He, J. Morel, Y. Xiong, *Water Res.* 46 (2012) 2299–2306.
- [33] L. Liu, T.D. Dao, R. Kodiyath, Q. Kang, H. Abe, T. Nagao, J. Ye, *Adv. Funct. Mater.* 24 (2014) 7754–7762.
- [34] E. Hosono, H. Matsuda, I. Honma, M. Ichihara, H. Zhou, *Langmuir* 23 (2007) 7447–7450.
- [35] C. Tsai, H. Teng, *Chem. Mater.* 18 (2006) 367–373.
- [36] Y. Suzuki, S. Yoshikawa, *J. Mater. Res.* 19 (2004) 982–985.
- [37] F. Alvarez-Ramirez, Y. Ruiz-Morales, *Chem. Mater.* 19 (2007) 2947–2959.
- [38] K.S.W. Sing, *Pure. Appl. Chem.* 57 (1985) 603–619.
- [39] Z. Chang, J. Liu, J. Liu, X. Sun, *J. Mater. Chem.* 21 (2010) 277–282.
- [40] E. Horváth, Á. Kukovecz, Z. Kónya, I. Kiricsi, *Chem. Mater.* 19 (2007) 927–931.
- [41] W. Su, J. Zhang, Z. Feng, T. Chen, P. Ying, C. Li, *J. Phys. Chem. C* 112 (2008) 7710–7716.
- [42] T. Ohsaka, F. Izumi, Y. Fujiki, *J. Raman. Spectroscopy* 7 (1978) 321–324.
- [43] M. Wei, Y. Konishi, H. Arakawa, *J. Mater. Sci.* 42 (2007) 529–533.
- [44] W. Göpel, G. Rocker, R. Feierabend, *Phys. Rev. B* 28 (1983) 3427.
- [45] H. Xia, J. Feng, H. Wang, M.O. Lai, L. Lu, *J. Power Sources* 195 (2010) 4410–4413.
- [46] W. Chen, P. Koshy, C.C. Sorrell, *Int. J. Hydrogen Energy* 40 (2015) 16215–16229.
- [47] M. Huang, Y. Zhang, F. Li, L. Zhang, R.S. Ruoff, Z. Wen, Q. Liu, *Sci. Rep.* 4 (2014).
- [48] J.G. Yu, X.J. Zhao, Q.N. Zhao, *Mater. Chem. Phys.* 69 (2001) 25–29.
- [49] A.B. Boffa, H.C. Galloway, P.W. Jacobs, J.J. Benítez, J.D. Batteas, M. Salmeron, A.T. Bell, G.A. Somorjai, *Surf. Sci.* 326 (1995) 80–92.
- [50] H. Xia, D. Zhu, Z. Luo, Y. Yu, X. Shi, G. Yuan, J. Xie, *Sci. Rep.* 3 (2013).
- [51] M. Kuang, T.T. Li, H. Chen, S.M. Zhang, L.L. Zhang, Y.X. Zhang, *Nanotechnology* 26 (2015) 304002.
- [52] S.U.M. Khan, M. Al-Shahry, W.B. Ingler, *Science* 297 (2002) 2243–2245.
- [53] Y. Cong, J. Zhang, F. Chen, M. Anpo, D. He, *J. Phys. Chem. C* 111 (2007) 10618–10623.
- [54] Q.J. Xiang, J.G. Yu, M. Jaroniec, *J. Phys. Chem. C* 115 (2011) 7355–7363.
- [55] J.A. Nav, O.G. Colón, M.A. Trillas, J. Peral, X. Domènech, J.J. Testa, J. Padrón, D. Rodr Guez, M.I. Litter, *Appl. Catal. B* 16 (1998) 187–196.
- [56] R. Vinu, G. Madras, *Environ. Sci. Technol.* 42 (2008) 913–919.
- [57] S. Wang, C. Chen, Y. Tzou, C. Hsu, J. Chen, C. Lin, *J. Hazard. Mater.* 164 (2009) 223–228.
- [58] W. Liu, T. Wang, A.G.L. Borthwick, Y. Wang, X. Yin, X. Li, J. Ni, *Sci. Total Environ.* 456–457 (2013) 171–180.
- [59] X.Z. Li, C.M. Fan, Y.P. Sun, *Chemosphere* 48 (2002) 453–460.
- [60] K. Wang, Y. Hsieh, M. Chou, C. Chang, *Appl. Catal. B* 21 (1999) 1–8.
- [61] M. Mullet, F. Demoisson, B. Humbert, L.J. Michot, D. Vantelon, *Geochim. Cosmochim. Acta* 71 (2007) 3257–3271.
- [62] D. Shuttleworth, *J. Phys. Chem.* 84 (1980) 1629–1634.
- [63] K.I. Ishibashi, A. Fujishima, T. Watanabe, K. Hashimoto, *Electrochem. Commun.* 2 (2000) 207–210.

- [65] E. Szabó-Bárdos, K. Somogyi, N. Törő, G. Kiss, A. Horváth, *Appl. Catal. B* 101 (2011) 471–478.
- [66] T. Wang, W. Liu, L. Xiong, N. Xu, J. Ni, *Chem. Eng. J.* 215–216 (2013) 366–374.
- [67] W. Liu, J. Ni, X. Yin, *Water Res.* 53 (2014) 12–25.
- [68] P. Bouras, E. Stathatos, P. Lianos, *Appl. Catal. B* 73 (2007) 51–59.
- [69] X. Fan, X. Chen, S. Zhu, Z. Li, T. Yu, J. Ye, Z. Zou, *J. Mol. Catal. A Chem.* 284 (2008) 155–160.
- [70] Y.J. Zhang, Y.C. Wang, W. Yan, T. Li, S. Li, Y.R. Hu, *Appl. Surf. Sci.* 255 (2009) 9508–9511.
- [71] J. Zhu, Z. Deng, F. Chen, J. Zhang, H. Chen, M. Anpo, J. Huang, L. Zhang, *Appl. Catal. B* 62 (2006) 329–335.
- [72] Q. Chen, W. Zhou, G. Du, L.M. Peng, *Adv. Mater.* 14 (2002) 1208–1211.
- [73] R. Ma, K. Fukuda, T. Sasaki, M. Osada, Y. Bando, *J. Phys. Chem. B* 109 (2005) 6210–6214.
- [74] N. Li, L. Zhang, Y. Chen, M. Fang, J. Zhang, H. Wang, *Adv. Funct. Mater.* 22 (2012) 835–841.
- [75] L. Xiong, Y. Yang, J. Mai, W. Sun, C. Zhang, D. Wei, Q. Chen, J. Ni, *Chem. Eng. J.* 156 (2010) 313–320.